Materials Today Bio 31 (2025) 101489

Contents lists available at ScienceDirect

Materials Today Bio

journal homepage: www.journals.elsevier.com/materials-today-bio

Cerium-based nanoplatform for severe acute pancreatitis: Achieving enhanced anti-inflammatory effects through calcium homeostasis restoration and oxidative stress mitigation

Tingyi Luo [a,c], Yujing Tang [b], Wangcheng Xie [a,c], Zhilong Ma [d], Jian Gong [c], Yonggui Zhang [e], Tingsong Yang [c], Xuyang Jia [c], Jia Zhou [f], Zhengyu Hu [g], Lin Han [h], Qigang Wang [b,i,**], Zhenshun Song [a,*]

[a] Department of Hepatobiliary and Pancreatic Surgery, Shanghai Fourth People's Hospital, School of Medicine, Tongji University, Shanghai, 200434, China
[b] School of Chemical Science and Engineering, Tongji University, Shanghai, 200092, China
[c] Department of Hepatobiliary and Pancreatic Surgery, Shanghai Tenth People's Hospital, School of Medicine, Tongji University, Shanghai, 200072, China
[d] Department of Pancreatic Surgery, Fudan University Shanghai Cancer Center, Shanghai, 200032, China
[e] Department of Critical Care Medicine & Emergency, Shanghai Chest Hospital, Shanghai Jiaotong University, Shanghai, 200030, China
[f] Department of General Surgery, Tongren Hospital, School of Medicine, Jiaotong University, Shanghai, 200335, China
[g] Department of Gastrointestinal and Hernia Surgery, The First Affiliated Hospital of Anhui Medical University, Anhui, 230000, China
[h] Central Laboratory, Shanghai Tenth People's Hospital, School of Medicine, Tongji University, Shanghai, 200072, China
[i] Shanghai Key Laboratory of Anesthesiology and Brain Functional Modulation, Clinical Research Center for Anesthesiology and Perioperative Medicine, Translational Research Institute of Brain and Brain-Like Intelligence, Shanghai Fourth People's Hospital, School of Medicine, Tongji University, Shanghai, 200434, China

ARTICLE INFO

Keywords:
Severe acute pancreatitis
Nanoplatform
Calcium
Oxidative stress
Mitochondrial dysfunction

ABSTRACT

Severe acute pancreatitis (SAP), a life-threatening inflammatory disease of the pancreas, has a high mortality rate (~40 %). Current therapeutic approaches, including antibiotics, trypsin inhibitors, fasting, rehydration, and even continuous renal replacement therapy, yield limited clinical management efficacy. Abnormally elevated calcium levels and reactive oxygen species (ROS) overproduction by damaged mitochondria are key factors in the inflammatory cascade in SAP. The combination of calcium chelators and cerium-based nanozymes loaded with catalase (MOF808@BA@CAT) was developed to bind intracellular calcium, eliminate excessive ROS, and ameliorate the resulting mitochondrial dysfunction, thereby achieving multiple anti-inflammatory effects on SAP. A single low dose of the nanoplatform (1.5 mg kg^{-1}) significantly reduced pancreatic necrosis in SAP rats, effectively ameliorated oxidative stress in the pancreas, improved mitochondrial dysfunction, reduced the proportion of apoptotic cells, and blocked the systemic inflammatory amplification cascade, resulting in the alleviation of systemic inflammation. Moreover, the nanoplatform restored impaired autophagy and inhibited endoplasmic reticulum stress in pancreatic tissue, preserving injured acinar cells. Mechanistically, the administration of the nanoplatform reversed metabolic abnormalities in pancreatic tissue and inhibited the signaling pathways that promote inflammation progression in SAP. This nanoplatform provides a new strategy for SAP treatment, with clinical translation prospects, through ion homeostasis regulation and pancreatic oxidative stress inhibition.

1. Introduction

Acute pancreatitis is a complex and common gastrointestinal disease with a varying clinical course that requires acute admission to the hospital and has an increasing overall incidence. The disease is characterized by pancreatic inflammation and considerable acinar cell damage, accompanied by a fast and systemic inflammatory response [1]. Approximately 20 % of patients with acute pancreatitis can develop to

** Corresponding author. School of Chemical Science and Engineering, Tongji University, Shanghai, 200092, China.
* Corresponding author. Department of Hepatobiliary and Pancreatic Surgery, Shanghai Fourth People's Hospital, School of Medicine, Tongji University, Shanghai, 200434, China.
E-mail addresses: wangqg66@tongji.edu.cn (Q. Wang), zs_song@tongji.edu.cn (Z. Song).

https://doi.org/10.1016/j.mtbio.2025.101489
Received 9 November 2024; Received in revised form 8 January 2025; Accepted 11 January 2025
Available online 13 January 2025

severe acute pancreatitis (SAP) with pancreatic or peripancreatic tissue necrosis, persistent organ failure, or both, with a mortality rate of up to 40 % [2,3]. Additionally, patients suffer from pancreatic exocrine and endocrine dysfunction after recovering from SAP [4,5]. Apart from conservative therapy, such as fluid resuscitation, nutritional support, the inhibition of pancreas secretion, and the prevention of infectious complications, there are no approved drugs that can effectively enhance SAP management, or improve patient prognosis. Thus, there is an urgent need for the development of treatments for SAP to promote survival, alleviate pancreatic damage and reduce the incidence of complications.

Pancreatic acinar cell (PAC) injury and the subsequent profound inflammatory cascade are the primary pathophysiological processes of SAP. Oxidative stress and reactive oxygen species (ROS) are closely associated with PAC damage [6,7]. Oxidative stress will cause a massive release of ROS, and activated ROS then triggers the nuclear factor kappa B (NF-κB) signaling pathway, initiating an inflammatory response and the release of inflammatory mediators. These events provoke an intense inflammatory response and ROS accumulation, which significantly amplify damage to the pancreas. Previous studies have shown that oxidative stress and subsequent mitochondrial damage to PAC are the main mechanisms of pancreas injury in SAP [8,9]. Thus, early and prompt elimination of ROS and control of oxidative stress and inflammation are crucial for inhibiting SAP progression.

PAC injury may be caused by multiple factors, such as abnormally elevated levels of calcium (Ca^{2+}) [5]. The inappropriate release of intracellular calcium can lead to cell necrosis and apoptosis, promote cell death and mediate inflammatory pathways, the activation of NF-κB and mitochondrial dysfunction [5,10,11]. We assume that the reduction of the toxic level of intracellular calcium in the early stage of SAP is effective in preventing the subsequent necrosis and apoptosis of PAC. The Ca^{2+} chelator, 1,2-bis (2-aminophenoxy) ethane-N,N,N, N′-tetraacetic acid (BAPTA-AM) is a hydrophobic membrane permeable calcium chelator with Ca^{2+}-binding capacity [12], can reduce intracellular Ca^{2+} by directly binding with Ca^{2+}. However, the hydrophobic characteristics of BAPTA-AM limit its direct application in cellular protection [13]. To address this issue, researchers have focused on the development of innovative nanodrug delivery systems engineered to increase the solubility of BAPTA-AM and prolong its biological half-life, maximizing its therapeutic potential.

In addition, mitochondrial dysfunction and impaired autophagy also contribute to PAC damage and pancreatic inflammation [8,11]. Our previous studies confirmed that mesenchymal stem cells (MSCs) attenuate SAP-related inflammation by delivering hypoxia-treated functional mitochondria to damaged PAC, confirming the critical role of mitochondrial dysfunction in SAP treatment [14]. Ca^{2+} overload or elevated ROS levels can result in the opening of the mitochondrial permeability transition pore (MPTP), which in turn leads to a reduction in the mitochondrial membrane potential (Δψm) and even cell death [11]. Mukherjee et al. reported that MPTP opening is critical for all forms of pancreatitis investigated [9]. Therefore, if both calcium levels and MPTP opening are inhibited, mitochondrial dysfunction in SAP may be effectively reversed, thus alleviating PAC necrosis.

Over the past few decades, progress in nanomedicine promoted the development in treating ROS-related inflammatory diseases through the use of functional nanoparticles (NPs) with free radical scavenging abilities, including ceria, platinum, and redox polymers [15]. Metal–organic frameworks (MOFs) are a class of porous hybrid nanomaterials constructed by the coordination of metal ion centers and organic ligands [16]. The meticulously crafted cavities and channels within their architecture are capable of creating hydrophobic coordination environments that closely mimic those found in natural enzymes [17]. By binding specific metal cations/clusters to organic ligands to establish catalytically active sites, MOF-based nanozymes with comprehensive ROS scavenging capabilities can be produced. Cerium (Ce) can be used as an antioxidant therapeutic drug as cerium-based nanozymes harness an exclusive redox oscillation between the Ce^{3+} and Ce^{4+} valence states, adeptly targeting and neutralizing ROS [18,19]. The inherent catalase, superoxide dismutase (SOD), oxidase, peroxidase and phosphatase mimetic properties of Ce NPs provide them superiority over a number of NPs [20]. Ce NPs have been found to be effective in treating conditions such as inflammation, rheumatoid arthritis, hepatic ischemia–reperfusion injury, and Alzheimer's disease [21,22]. Amit Khurana et al., reported that nanoceria with catalase and SOD can mitigate pancreatitis-associated inflammation, in vitro and in vivo [23]. Further, the administration of nanoceria significantly reduce the inflammatory signaling, and attenuated the fibrogenesis and epithelial-to-mesenchymal transition during chronic pancreatitis [24]. These existing evidences suggested that Ce NPs are a potential therapeutic option for pancreatitis. However, in dealing with intricate diseases, such as SAP, where the internal ROS levels are abnormally high and complex, the performance of individual nanozymes has several limitations. Therefore, how to fully explore and enhance the antioxidant potential of nanozymes to more effectively combat the ROS storm has become an urgent scientific challenge.

Considering these findings, we developed a cerium-based nanoplatform, MOF808@BA@CAT, to achieve enhanced anti-inflammatory effects on SAP. MOF808 particles were synthesized via a hydrothermal method and serve as antioxidant enzymes with remarkable ROS-scavenging ability. Concurrently, MOF808 was utilized as the core of a composite system to carry BAPTA-AM for Ca^{2+} chelation. Considering the cascade of amplified inflammatory effects caused by large amounts of ROS in SAP, catalase (CAT) was anchored onto the MOF808 scaffold by employing supramolecular assembly techniques (MOF808@BA@CAT), which afforded the system enhanced antioxidant therapeutic effects. In vitro, MOF808@BA@CAT effectively reduced the intracellular calcium level and decreased mitochondrial dysfunction and cell apoptosis, which alleviated the inflammatory response after excessive oxidative stress stimulation. In a rat SAP model, MOF808@BA@CAT, which has powerful enzymatic activity, effectively ameliorated oxidative stress, decreased systemic inflammatory levels and alleviated pancreatic tissue damage, exerting a protective effect on SAP. This nanoplatform, MOF808@BA@CAT, can provide a potent strategy for SAP treatment and has great potential for improving SAP outcomes (see Scheme 1).

2. Materials and methods

2.1. Materials

Cerium ammonium nitrate $(NH_4)_2[Ce(NO_3)_6]$ (CAN), N,N-dimethylformamide (DMF), 1,3,5-benzenetricarboxylic acid (H_3BTC), formic acid, were purchased from Aladdin (Shanghai, China). The SOD assay kit and superoxide anion assay kits were obtained from Nanjing Jiancheng Biological Engineering Institute (Nanjing, China). Catalase (CAT) was purchased from Sigma-Aldrich, USA. BAPTA-AM (BA) was purchased from MedChemExpress. $[Ru(dpp)_3]Cl_2$ was acquired from Shanghai Maokang Biotechnology Co. Ltd (Shanghai, China). Xanthine oxidase, xanthine, 2,2′-azino-bis (3-ethylbenzothiazoline-6-sulfonic acid) (ABTS) and 2,2-diphenyl-1-picrylhydrazyl (DPPH) were purchased from Shanghai Yuanye Bio-Technology Co., Ltd (Shanghai, China). $FeSO_4$, $Ti(SO_4)_2$, H_2O_2 and $K_2S_2O_8$ were acquired from Sinopharm Chemical Reagent Co., Ltd (Shanghai, China). All reagents were used as purchased without further purification.

2.2. Synthesis of MOF808 nanoparticles (MOF808 NPs)

MOF808 was synthesized through a hydrothermal method according to reported procedure [25,26], employing a reaction medium that contained a cerium-based salt as the metal source, the protonated form of an organic ligand to act as the linking component, and formic acid utilized as a structure-directing modulator. Briefly, to a solution of H_3BTC (67.2 mg) in 1.6 mL of DMF, HCOOH (4.12 mL) and $(NH_4)_2$[Ce

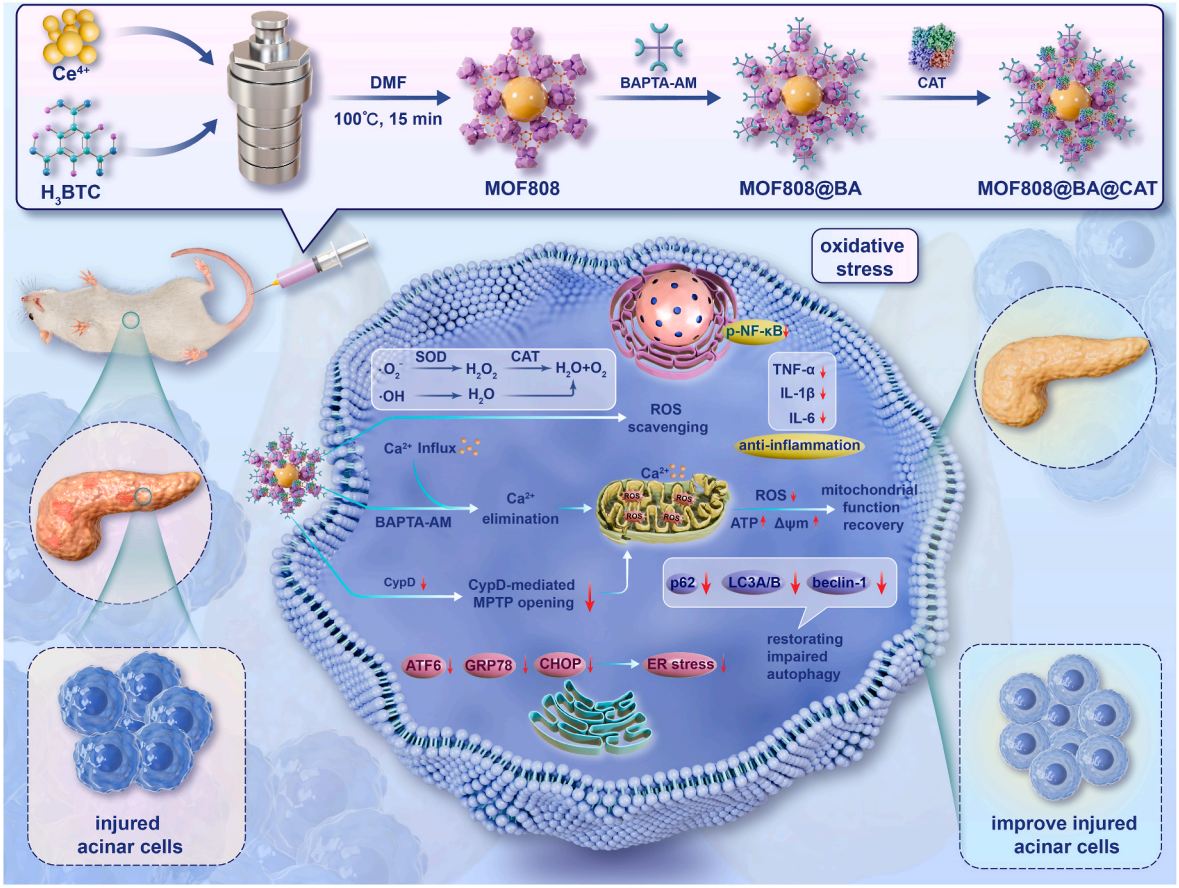

Scheme 1. Schematic illustration of the synthetic route of cerium-based nanoplatform MOF808@BA@CAT and its anti-oxidative and anti-inflammatory effects on SAP (Created with Figdraw).

$(NO_3)_6$] (0.533 M, 1.2 mL) were added successively. After mild stirring for 5 min, the solution was introduced into a Teflon lined hydrothermal autoclave, followed by a heating reaction at 100 °C for 15 min to obtain the precipitate. After cooling to room temperature, the precipitate was centrifuged twice in DMF and twice in acetone. The resulting powder was dried under vacuum at 60 °C and labeled MOF808. BAPTA-AM (BA, 0.5 mg) and MOF808 (0.5 mg) were fully dispersed in separate solutions of DMSO (2 mL) and then mixed and stirred for 1 h. The mixture was subjected to centrifugation and washed three times at 14,000 rpm for 8 min to eliminate the remaining DMSO. The resulting product was then freeze-dried, yielding MOF808@BA. 1 mg of MOF808 or MOF808@BA was dispersed in 1 mL of PBS and mixed with 0.2 mg of CAT dissolved in 2 mL of neutral PBS under stirring. After 6 h of stirring, the resulting product was collected by centrifugation at 14,000 rpm for 8 min while washing with PBS three times. The resulting product was then freeze-dried and coded as MOF808@CAT or MOF808@BA@CAT, respectively.

2.3. Characterization of MOF808 nanoparticles

Images from transmission electron microscopy (TEM) and energy-dispersive X-ray spectroscopy (EDS) were obtained via a JEM-2100 microscope operated at 200 kV (manufactured by JEOL, Japan). Scanning electron microscopy (SEM) observations were conducted with an S-4800 instrument from Hitachi, Japan. A Magellan 400 L system (supplied by FEI, USA) was used for scanning transmission electron microscopy (STEM) and elemental mapping. Ultraviolet–visible (UV–vis) absorption spectra were recorded on a UV-2700 spectrophotometer (Shimadzu, Japan). Fourier-transform infrared (FT-IR) spectra were measured with a Nicolet iS10 infrared spectrophotometer (Thermo Fisher Scientific, USA). X-ray photoelectron spectroscopy (XPS) was conducted via an ESCALab250Xi electron spectrometer with an Al Kα X-ray radiation source (Thermo Fisher Scientific, USA). The N_2 adsorption/desorption isotherms were determined via a Micromeritics Tristar II 3020 apparatus. The crystalline phase of the synthesized products was scrutinized through X-ray diffraction (XRD) analysis performed on a Rigaku D/MAX RINT-2000 X-ray diffractometer. Electron paramagnetic resonance (EPR) measurements were conducted using a 100G-18KG/EMX-8/2.7 electron−spin resonance spectrometer.

In order to investigate the drug loading capacity, we conducted an exploration of different ratios of MOF808 to BA (1:0.1, 1:0.25, 1:0.5, 1:0.75, 1:1). After reacting in DMSO for 1 h, the supernatant was collected by centrifugation at 13,000 rpm for 8 min. The supernatant obtained was employed for determining the concentration of the unencapsulated drug via high-performance liquid chromatography (HPLC, Agilent 1260). The chromatographic separation was achieved using a mixture of acetonitrile and water in a ratio of 3:2 (volumetric), supplemented with 0.1 % trifluoroacetic acid as mobile phases. The loading capacity (LC%) and encapsulation efficiency (EE%) of BA were ascertained using the following formulas, respectively.

$$LC(\%) = \frac{weight\ of\ encapsulated\ BA}{total\ weight\ of\ NPs} \times 100\%$$

$$EE(\%) = \left(1 - \frac{weight\ of\ free\ BA}{total\ weight\ of\ BA}\right) \times 100\%$$

2.4. Evaluation of $\bullet O_2^-$ clearance ability

The ability to quench superoxide anion radicals ($\bullet O_2^-$) was

investigated via a colorimetric SOD assay kit. After incubation for 30 min with the MOF808 at various concentrations (10, 15, 20, 50, 100, 200 μg mL^{-1}), a chromogenic agent was added to test for changes in absorbance at 550 nm. The capacity to neutralize $\bullet O_2^-$ was assessed via EPR spectroscopy. Superoxide anions were generated at room temperature from a reaction involving xanthine and xanthine oxidase. Both MOF808 and MOF808@CAT, each at a concentration of 200 μg mL^{-1}, were subsequently introduced into the superoxide radical solution and allowed to incubate for an additional 30 min. DMPO was incorporated into the mixture as a spin trapping agent, and the EPR technique was utilized to evaluate the samples' efficacy in scavenging the superoxide anion radicals.

2.5. Evaluation of •OH and H_2O_2 scavenging ability

The hydroxyl radical (•OH) scavenging ability was evaluated via the salicylic acid (SA) method and a UV–visible spectrophotometer. The hydroxyl radicals were generated via the Fenton reaction involving 10 mM $FeSO_4$ and 100 mM H_2O_2. Various concentrations of MOF808 and MOF808@CAT (2, 10, 20, 50, and 100 μg mL^{-1}) were introduced into the solution. The remaining hydroxyl radicals were quantified by measuring the characteristic absorption peak of 2,3-dihydroxybenzoic acid at 510 nm, which indicated the extent of the reaction between the hydroxyl radicals and salicylic acid. The •OH scavenging abilities of the synthesized MOF808 and MOF808@CAT were assessed via electron spin resonance (ESR) spectroscopy at ambient temperature.

We determined the content of H_2O_2 via the titanium sulfate colorimetric method, and thus calculated the material's ability to clear H_2O_2. Different concentrations (2, 10, 20, 50, and 100 μg mL^{-1}) of MOF808 and MOF808@CAT were co-incubated with H_2O_2 (1 mM) for 5 min, then mixed with a $Ti(SO_4)_2$ solution (80 mM, prepared by mixing 10 mL of H_2SO_4 with 40 mL of deionized water). Using the blank control group as a basis, the concentration and clearance rate of H_2O_2 were determined by measuring the absorbance at 410 nm. When we independently assessed the ability of different concentrations (5, 10, 20, 50, 100, and 200 μg mL^{-1}) of MOF808 to decompose H_2O_2 within 1 h, we employed the same method as described above, with the only difference being the incubation time.

2.6. Evaluation of DPPH and ABTS free radical scavenging activity

1 mM ethanolic solution of DPPH was blended with the sample solutions at varying concentrations (10, 20, 50, 100, and 200 μg mL^{-1}). The mixtures were then incubated in the dark for a duration of 30 min to allow for the reaction to take place. After incubation, the absorbance of each solution was measured spectrophotometrically at a wavelength of 517 nm. The procedure involved the generation of ABTS free radicals (ABTS•) by reacting an ABTS stock solution (7.4 mM, 0.4 mL) with potassium persulfate ($K_2S_2O_8$, 0.0025 g) in water (3.575 mL) for a period of 12 h, following a well-established protocol. Various concentrations of MOF808 and MOF808@CAT were subsequently introduced into the ABTS• radical solution. The mixtures were then subjected to UV–vis–NIR spectroscopic analysis to monitor the absorption changes at 734 nm, which indicate the extent of ABTS• scavenging by the materials.

2.7. Evaluation of the oxygen-generating capability

First, to each well containing a solution with 10 μL of 250 mM H_2O_2 and 100 μL of 10 μM $[Ru(dpp)_3]Cl_2$ luminescent oxygen sensor, we added 40 μL of MOF808 or MOF808@CAT, each at a concentration of 50 μg mL^{-1}. The fluorescence spectrum was immediately detected via a multifunctional microplate reader with an excitation wavelength (Ex) set at 455 nm. The excitation wavelength was subsequently set to 455 nm, and the changes in fluorescence intensity over time at an emission wavelength of 633 nm were continuously monitored. Finally, to each well, we added varying final concentrations of MOF808@CAT (10, 20, 50, 100, 200 μg mL^{-1}) and a fixed concentration of MOF808 (200 μg mL^{-1}). With the excitation wavelength maintained at 455 nm, we examined the differences in fluorescence intensity at an emission wavelength of 633 nm.

2.8. Isolation and characterization of rat primary pancreatic acinar cell

Methods for isolation of primary pancreatic acinar cell have been described in detail previously [27,28]. In brief, 4 weeks old healthy SD rats were euthanized and disinfected by immersion in 75 % ethanol for 15 min. The abdomen was opened to collect fresh pancreas. The pancreatic lobes were dissected into small pieces and transferred to HBSS media (H1025, Solarbio, China) containing 2 mg mL^{-1} of type IV collagenase (17104019, Gibco, USA). The tissue was vigorously shaken for 25 min at 37 °C to maximize homogeneous digestion of the pancreatic tissue. The digestion was terminated using HBSS containing 5 % FBS (A5669701, Gibco, USA), and filtered through a 100 μm sieve. Then, the supernatant was removed by centrifugation and the cell pellet was resuspended in Waymouths medium (PM151215, Pricella, China) containing 1 % FBS, 0.1 mg mL^{-1} of soybean trypsin inhibitor (T9003, Sigma-Aldrich, Germany) and 1 % penicillin/streptomycin (15140122, Gibco, USA). The nonadherent PAC were transferred into a T25 cell culture flask for 24 h for subsequent analyses.

2.9. Cellular uptake and cell viability evaluation

PAC were stimulated with H_2O_2 (200 μM) to simulate inflammatory injury. FITC-labeled MOF808 (10 μg mL^{-1}) and MOF808@BA@CAT (10 μg mL^{-1}) were respectively added to each well for a 24 h incubation. PAC nuclei were stained with Hoechst 33342 (C1028, Beyotime, China) for 10 min, while the cell membrane was stained with DiI (C1036, Beyotime, China). Finally, after washing with PBS, the fluorescence images were acquired via a confocal fluorescence microscopy (CLSM780, Carl Zeiss, Germany).

PAC were incubated with H_2O_2 (200 μM), MOF808 (10 μg mL^{-1}) or MOF808@BA@CAT (10 μg mL^{-1}) + H_2O_2 (200 μM) for 24h. The cytoprotective effects of the formulations were measured via CCK-8 kits. To evaluate the cell survival status, the cells were subjected to Calcein/PI (C2015S, Beyotime, China) staining. After a 30 min incubation, the cells were washed with PBS. Fluorescence images were captured via an inverted fluorescence microscope.

2.10. Detection of intracellular calcium levels and ROS levels

To evaluate the Ca^{2+}-scavenging ability of MOF808 NPs, PAC were stimulated following the procedures outlined previously. After 24 h of incubation with MOF808 (10 μg mL^{-1}) and MOF808@BA@CAT (10 μg mL^{-1}), the cells were incubated with a Fluo-4 AM probe (S1060, Beyotime, China) for 30 min. Then, the cells were collected after being washed with PBS, and the relative calcium levels were evaluated via flow cytometry.

The intracellular levels of ROS were assessed by using DCFH-DA (50101ES01, Yeasen, China) as an indicator. DCFH-DA (100 μM) was added, and the cells were incubated for 30 min. After the cells were washed with PBS, images of each well were obtained via fluorescence microscopy. The mean fluorescence intensity in random vision fields was quantified via ImageJ software. Moreover, flow cytometry was also used to quantify the intracellular ROS level. The cells were seeded in a 6-well plate (5×10^5 cells/well). The same treatment was performed for fluorescence imaging. Then, the cells were collected and centrifuged, and the cell suspensions were collected for further flow cytometry analysis.

2.11. Quantitative real-time PCR (qRT–PCR)

qRT−PCR was used to detect the relative mRNA expression levels of

inflammatory cytokines (IL-1β, IL-6, IL-10 and TNF-α) in PAC. The total RNA of the PAC in each group was extracted via an RNA-Quick extraction kit (RN001, Yishan Biotechnology, China) according to the manufacturer's instructions, and reverse transcription of the mRNAs was performed via the PrimeScript RT Reagent Kit (RR037A, Takara, Japan). The primers (Table S1) were designed and synthesized by Sangon Biotech (Shanghai, China). Through the application of SYBR Green reagent (11202ES08, Yeasen, China), the gene expression levels were detected via the QuantStudio Dx PCR system. Gene expression levels in all samples were normalized via the $2^{-\Delta\Delta Ct}$ method with Actin used as an internal control for comparison.

2.12. Cell apoptosis analysis

PAC were digested with EDTA-free trypsin to prepare single-cell suspensions. Then, PI solution and Annexin-V FITC dye were added to the binding buffer (0.4 mL) for cell staining, and the mixture was incubated for 15 min in the dark. Apoptosis analysis was performed via flow cytometry. Quantitative analysis of the flow cytometry data was conducted on the average fluorescence of selected cell populations via Flow Jo software.

2.13. Mitochondrial superoxide (mito SOX) and mitochondrial membrane potential assay

The cells were collected by centrifugation and then resuspended in a preconfigured Mito SOX (S0061S, Beyotime, China) working solution (1.0 mL, 5 μM) for 30 min at 37 °C. The nuclei were stained with Hoechst for 10 min. Then, the cells were observed and photographed via confocal fluorescence microscopy. The mean fluorescence intensity in random vision fields was quantified via ImageJ software.

PAC were incubated with JC-1 (C2006, Beyotime, China) staining working solution in the dark for 30 min at 37 °C and washed three times with staining buffer. The fluorescence images were captured via confocal microscopy. The relative fluorescence intensity of JC-1-Red/Green was quantified via ImageJ software. Moreover, flow cytometry was also used to detect cells with low mitochondrial membrane potential.

2.14. Animal experimental SAP and follow-up treatment

All animal experiments were performed in accordance with the National Institutes of Health Guide for the Care and Use of Laboratory Animals and were approved by the Animal Ethics Committee of Shanghai Tenth People's Hospital (approval number: SHDSYY-2023-2330). Male SD/SPF rats (6 weeks-of-age) were provided by Charles River Laboratory (Beijing, China) and were acclimatized at the Animal Center of the Shanghai Tenth People's Hospital for 7 days prior to the experiment and fasted for 12 h prior to surgery. The SAP model was constructed by retrograde biliopancreatic duct injection of 3 % NaT. MOF808 (1.5 mg kg^{-1}) and MOF808@BA@CAT (1.5 mg kg^{-1}) were injected via the tail vein at 6 h following the induction of 3 % NaT. The control group was injected with an equal volume of solvent vehicle. Then, 48 h after the induction of SAP, the rats were euthanized and the pancreatic tissue, blood and other organs were harvested for subsequent experiments.

Cyanine5.5-labeled MOF808@BA@CAT was constructed according to the instructions of Cyanine5.5 (210892-23-2, MedChemExpress, USA). The rats were photographed vis a multimodal animal live imaging system (AniView100, China) at various time intervals.

2.15. Histopathology

Rat pancreatic and lung tissue was collected and fixed in 4 % paraformaldehyde for 48 h, gradient dehydrated, and embedded in paraffin for sectioning. Slices were stained with hematoxylin and eosin. Two experienced pathologists scored the degree of pancreatic damage according to a previous scale in a double-blinded manner (Table S2).

2.16. Detection of biochemical indicators in serum and cerium content in tissues

The serum amylase level of the rats was analyzed via commercial kits (C033, Changchun Huili, China) in accordance with the manufacturer's instructions. The levels of MDA in pancreatic tissue were detected by via a lipid peroxidation MDA assay kit (G4300, Servicebio, China). The SOD-like activity, CAT-like activity and the levels of reduced GSH in pancreatic tissue were detected by using the manufacturer's assay kit (G4306, G4307, G4305, Servicebio, China). The serum levels of IL-1β (EK301B, MULTI SCIENCES, China), IL-6 (EK306, MULTI SCIENCES, China) and TNF-α (EK382, MULTI SCIENCES, China) in each group were measured via ELISA kits according to the manufacturers' instructions. The cerium metal in pancreas tissue was analyzed by inductively coupled plasma-mass spectrometry (ICP-MS). The pancreas from the MOF NPs-treated groups were collected, and digested in nitric acid (1 mL) and hydrogen peroxide (0.5 mL), and then the samples were heated and digested at 120° in an oven for 30 min. After cooling, the volume was fixed. According to the operating procedures, the content of the standard samples and the samples to be tested were detected by Perkin Elmer NexION 300D ICP-MS (Perkin Elmer, USA).

2.17. Transmission electron microscopy (TEM)

Pancreatic tissue was fixed in 2.5 % glutaraldehyde at 4 °C for 2 h. After being washed three times with 0.1 M phosphate buffer and fixed in 1 % osmic acid at 4 °C for 2 h, the pancreatic tissue was gradient dehydrated in a graded series of ethanol. Next, the samples were embedded in Epon-Araldite resin for penetration and placed in a mold for polymerization. After the semithin sections were used for positioning, ultrathin sections were made and collected for microstructure analysis. The sections were counterstained with 3 % uranyl acetate and 2.7 % lead citrate. The samples were then observed via a JEM1400 transmission electron microscope.

2.18. Immunohistochemical staining and immunofluorescence assay

Paraffin-embedded tissue samples were cut into 4 μm-thick sections, which were dewaxed and dehydrated. Following antigen repair, the sections were blocked with goat serum for 1 h and incubated with antibodies against MPO (1:500 dilution, 22225-1-AP, Proteintech, China), followed by incubation with a goat-anti-rabbit secondary antibody (G1213, Servicebio, China). The tissue sections were subsequently stained with 3,3′-diaminobenzidine and hematoxylin. Images were acquired via optical microscopy.

The cells or tissues were permeabilized with 0.1 % Triton X-100 for 10 min, blocked with goat serum for 1 h, and incubated with anti-HMGB1 (1:100 dilution, T55060, Abmart, China), anti-TOM20 (1:500 dilution, 11802-1-AP, Proteintech, China) or anti-CypD (1:100, 18466-1-AP, Proteintech, China) antibodies overnight at 4 °C. The next morning, the sections were incubated for 2 h at room temperature with an AF488-conjugated secondary antibody. The cell nuclei were restained with DAPI. Fluorescence images were acquired via confocal fluorescence microscopy.

2.19. Western blotting

Pancreatic tissue or cells were lysed in radio immunoprecipitation assay lysis buffer (RIPA, PC101, Epizyme, China) containing 1 % protease inhibitor (GRF101, Epizyme, China) at 4 °C. The same amount of each protein sample was separated via electrophoresis and transferred to nitrocellulose filter membranes. The membranes were blocked with 5 % milk in TBST for 1 h at room temperature and then incubated with

primary antibodies (Table S3) overnight at 4 °C. Afterward, the membranes were washed and incubated with the secondary antibody for 1 h at room temperature. Immunoreactive protein bands were visualized with an enhanced chemiluminescence system (Amersham Imager 600; GE Healthcare Bio-Sciences Corp., USA), and the bands were analyzed for grayscale values via ImageJ software.

2.20. Metabolomics analysis and RNA sequencing

The pancreatic tissue (100 mg) was ground with liquid nitrogen and transferred to a microcentrifuge tube with 500 μL of cold methanol, vortexed and shaken, left to stand in an ice bath for 5 min, and centrifuged at 15,000×*g* for 20 min at 4 °C. Next, 300 μL of the supernatant was diluted with mass spectrometry grade water to 53 % methanol, centrifuged at 15,000×*g* for 20 min at 4 °C, and the supernatant was collected for analysis via ultrahigh-performance liquid chromatography coupled with mass spectrometry (UHPLC/MS). The UHPLC-MS/MS assay was performed via a Vanquish UHPLC system (Thermo Fisher, Germany) coupled with an Orbitrap Q Exactive™ HF mass spectrometer or Orbitrap Q Exactive™ HF-X mass spectrometer (Thermo Fisher, Germany) at Novogene Co., Ltd. (Beijing, China). Raw data (.raw) files were imported into Compound Discoverer 3.3 (CD 3.3, Thermo Fisher) software for processing. To further characterize the metabolic changes and pathways involved, individual metabolites were processed and analyzed via the NovoMagic cloud platform (https://magic-plus.novogene.com/#/). Pathway analysis and enrichment analysis were based on the KEGG pathway database.

The preparation and sequencing of the RNA-seq libraries were performed by Novogene Co., Ltd. (Beijing, China). Total RNA was extracted from PAC via TRIzol reagent, and cDNA libraries for RNA-seq analysis were then prepared via an Illumina NEBNext UltraTM RNA Library Prep Kit. Universal bridging substrates were ligated to cDNA fragments, and the quality of the sequencing libraries was tested via the Bioanalyzer 2100 system (Agilent Technologies, CA, USA). The constructed cDNA libraries were sequenced on the HiSeq 2000 platform (TruSeq SBS KIT-HS V3, Illumina), with paired ends sequenced to 150 bp. Gene expression levels were determined, and differentially expressed genes (DEGs) were further identified.

2.21. Statistical analysis

Statistical analyses were performed via GraphPad Prism (V 10.0, San Diego, CA) and R (v4.1.1, New Zealand). The data are expressed as the means ± standard deviations (SDs). Two-tailed t_tests and one-way analysis of variance (ANOVA) followed by Tukey's test were used for comparisons. The results were considered significant when $p < 0.05$.

3. Results

3.1. Preparation and characterization of MOF808 NPs

MOF808 was successfully synthesized through a solvothermal method using ammonium cerium (IV) nitrate as the metal ion source, 1,3,5-benzyleric acid (H_3BTC) as the organic linker, and formic acid as a structure-directing modulator. The complete synthesis process of the MOF808 NPs is shown in Fig. 1A.

After BA loading and CAT conjugation, the resulting particles (MOF808@BA@CAT) retained their spherical morphology, in accordance with the morphology of the as-synthesized native MOF808 NPs (Fig. 1B and C), which were slightly smaller than the hydration radius (Fig. 1D). Moreover, MOF808 was predominantly composed of spherical nanoparticles with a uniform size of 50–100 nm and homogeneously distributed C, O, and Ce (Fig. 1E). The zeta potentials of MOF808, MOF808@BA and MOF808@BA@CAT suspended in water were ~-26.9, −9.1 and −18.7 mV, respectively (Fig. 1F), confirming the successful modification of the nanomaterial.

The surface composition of the MOF808 NPs was further investigated via X-ray photoelectron spectroscopy (XPS). The survey scan spectra revealed the presence of C, O, and Ce in the obtained MOF808 (Fig. 1G). The Ce 3d XPS spectrum of MOF808 exhibited five peaks corresponding to the spin–orbit splitting of the Ce (IV) $^3d_{5/2}$ and $^3d_{3/2}$ orbitals and three peaks corresponding to the spin–orbit splitting of the Ce (III) $^3d_{5/2}$ and $^3d_{3/2}$ orbitals (Fig. 1H), which implied the simultaneous presence of both Ce^{4+} and Ce^{3+} oxidation states within the fabricated nanostructures. The binding energies of Ce^{4+} (red anchor) were 916.86 eV, 908.40 eV, 900.80 eV, 887.65 eV, and 883.71 eV, and those of Ce^{3+} (blue anchor) were 904.70 eV, 885.92 eV, and 882.32 eV. The C1s XPS spectra exhibited a distinct peak at 288.2 eV and sp^2-bonded carbon C═C peak at 284.8 eV. The C1s peak at 288.2 eV was attributed to the O—C═O groups (Fig. 1I). The O1s XPS signature of MOF808 revealed three discrete peaks, as illustrated in Fig. 1J. These peaks corresponded to distinct oxygen environments within the Ce6 clusters and the H_3BTC ligands: the first peak was associated with oxygen atoms in the free carboxyl groups of H_3BTC (O-C═O) at a binding energy of 533.35 eV, and the second peak corresponded to the oxygen atoms in the carboxylate groups coordinated to the Ce6 cluster (Ce-O-C) at 530.48 eV [29, 30]. Additionally, the O1s XPS spectrum indicated a significant peak at 531.78 eV, which was attributed to unsaturated Ce-OH groups. The higher intensity of this peak among the three O1s signal peaks suggested the presence of many Ce-OH reactive sites on the MOF808 surface. The specific surface area of MOF808 was determined to be ≈ 49.8829 m^2g^{-1} and the pore sizes were calculated to be ~5.3 nm based on Brunauer−Emmett−Teller (BET) (Fig. 1K–Table S4, Fig. S1). The powder X-ray diffraction (XRD) pattern of MOF808 revealed a high degree of crystallinity, which was consistent with the reported PXRD pattern (Fig. 1L), verifying that MOF808 was successfully prepared.

Fig. 1M provides visual confirmation of the presence of CAT in the MOF808 composite through the identifiable amide I peak in the 1700–1600 cm^{-1} spectral region. The second derivative spectra shown in Fig. 1N suggested a substantial alteration in the spectral bands related to the protein content, indicating a deviation from the pure CAT enzyme spectrum. The ATR-FTIR spectrum of CAT was characterized by the vibrational peaks of the amide I bands at 1687, 1654, and 1636 cm^{-1}, and the amide II bands at 1545 and 1618 cm^{-1}, which are marked by gray dashed lines [31]. A bicinchoninic acid (BCA) assay of the supernatant was used to determine the concentration of CAT that had been conjugated to the particles (Figs. S2–4). It can be clearly observed that after reacting different ratios of MOF808 with CAT and analyzing the supernatant, the content of CAT in the supernatant is almost negligible. Additionally, the UV absorption spectrum of the MOF808@BA nanoparticles in DMSO displayed a peak at approximately 289 nm (Fig. S5), a feature that closely resembles the characteristic absorption peak of BA. The absence of this feature in the blank MOF808 NPs indicated that the drug was effectively encapsulated within the carrier system. In addition, the mass ratio of MOF808 to BA decreases from 1:0.1 to 1:1 (Fig. S3), the loading capacity (LC%) of BA increases accordingly, reaching a loading capacity of up to 47 % (Fig. S7). These results indicated the method we proposed to construct MOF808@BA@CAT is effective.

3.2. Free radical scavenging ability in vitro

Cerium can switch between two oxidation states, Ce(III) and Ce(IV), which enables cerium to neutralize ROS, thereby mimicking the function of natural antioxidant enzymes. Given that BA loading does not affect the enzyme activity of MOF808, we evaluated the ROS scavenging activity of MOF808. The ability of MOF808 to scavenge $\bullet O_2^-$, H_2O_2, and •OH, which are representative ROS involved in SAP, was then investigated. The results suggested that MOF808 presented concentration-dependent elimination of H_2O_2 and $\bullet O_2^-$ (Fig. 2A, Fig. S8). The ability to neutralize DPPH radicals indicates the presence of antioxidants that can donate electrons or hydrogen atoms to stabilize free radicals. MOF808 had a dose-dependent effect on the DPPH scavenging capacity

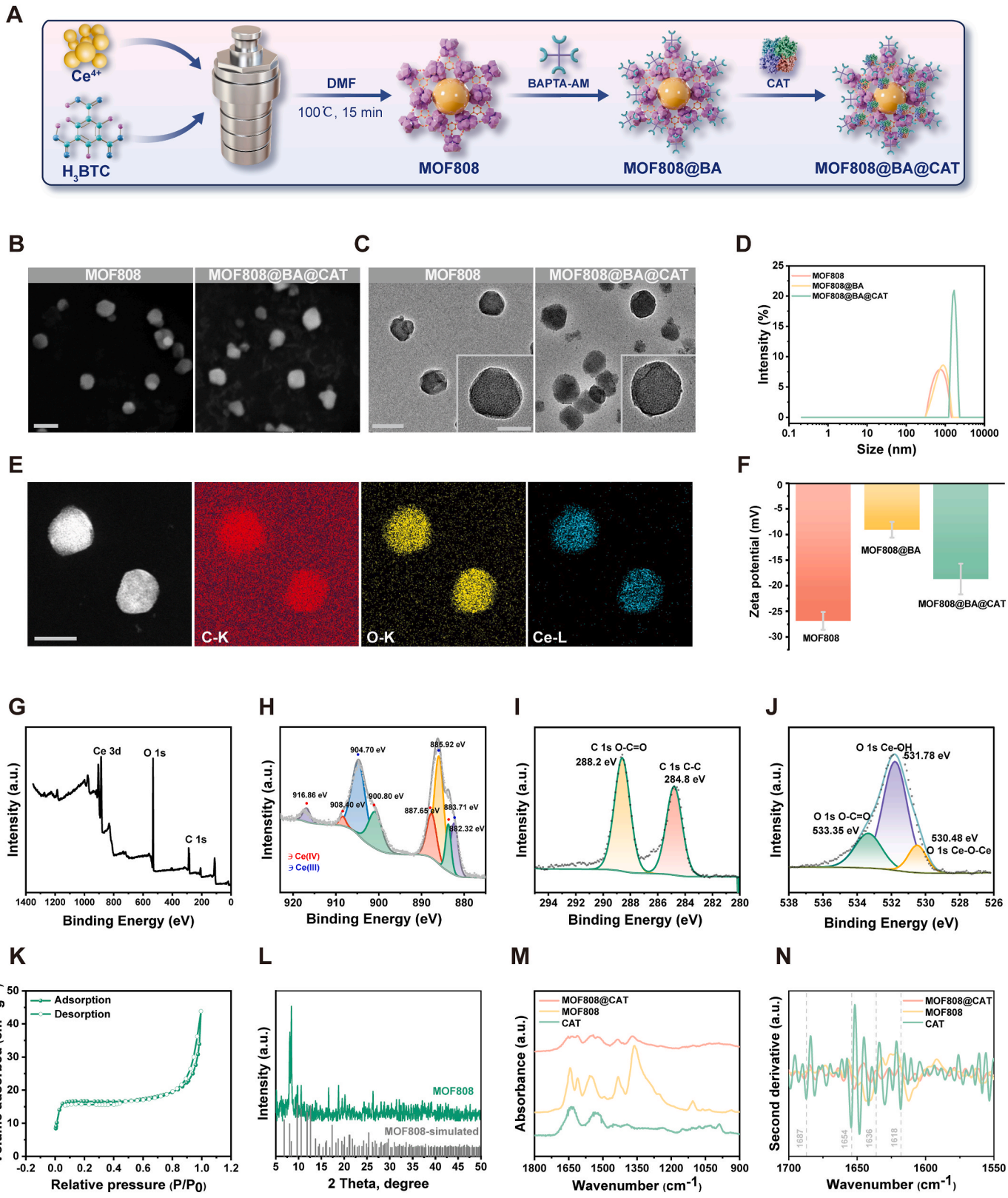

Fig. 1. Preparation and characterization of MOF808 NPs

A) Schematic diagram of MOF808@BA@CAT synthesis progression. B) The scanning electron microscopy and C) the transmission electron microscopy images of MOF808 NPs. Scale bar = 100, 50 nm. D) Hydrodynamic diameter and F) zeta potential of MOF808 NPs. E) EDS elemental mapping images of MOF808. Scale bar = 50 nm. G-J) X-ray photoelectron spectroscopy spectra of MOF808 G) and high-resolution XPS patterns of H) Ce 3d, I) C 1s and J) O 1s peaks of MOF808. K) The N2 sorption isotherm of MOF808. L) The powder X-ray diffraction (XRD) patterns of simulated MOF808 and as-synthesized MOF808. M, N) Attenuated total reflection Fourier-transform infrared (ATR-FTIR) spectra and the corresponding second derivative ATR-FTIR spectra of MOF808 NPs.

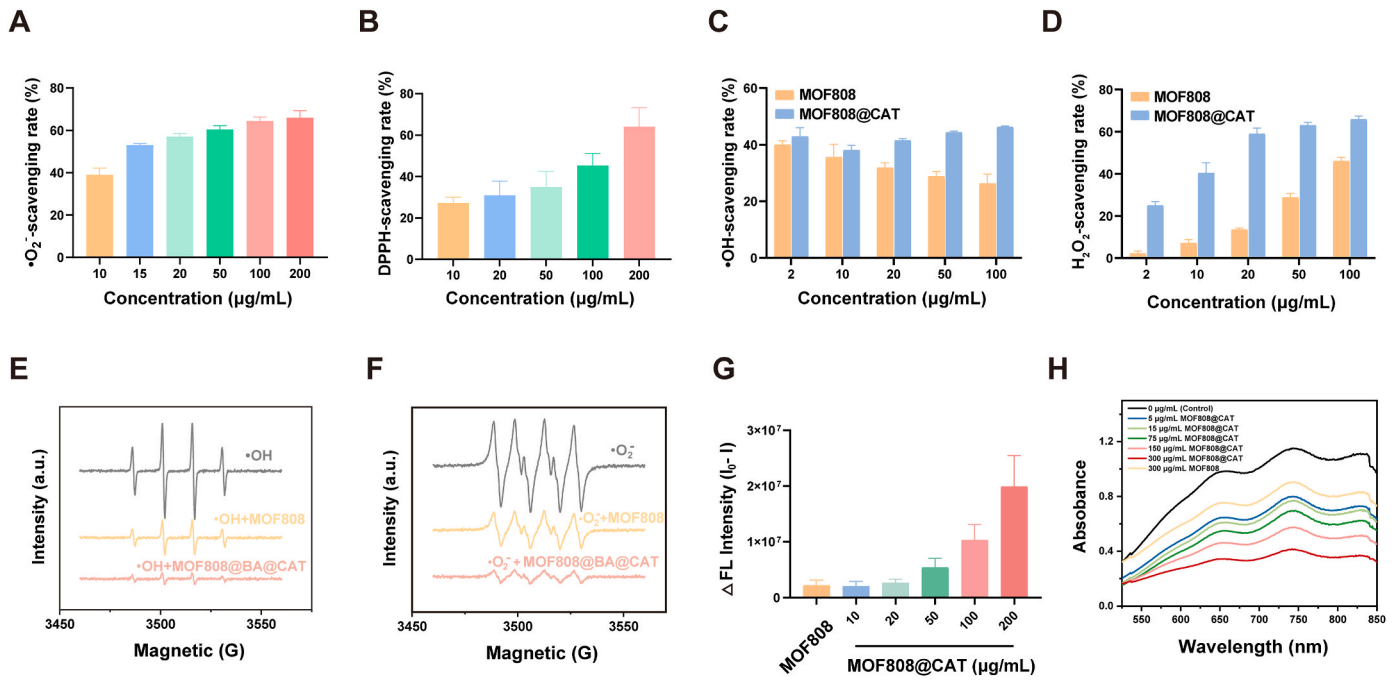

Fig. 2. Free radical scavenging performances in vitro.
A) The $\bullet O_2^-$ B) and DPPH clearance rate of MOF808 at different concentrations ($n = 3$). C The •OH D) and H_2O_2 clearance rate of MOF808 and MOF808@CAT at different concentrations ($n = 3$). E-F) The ESR spectra of MOF808 and MOF808 @CAT for •OH scavenging E) and $O_2^{\bullet-}$ scavenging F). G) Fluorescence intensity analysis of O_2 generation with different treatment, Ex = 455 nm, Em = 633 nm ($n = 3$). H) UV–vis absorption spectra of MOF808 and MOF808@CAT and $ABTS^{\bullet}$ after incubation with different concentration gradients.

and achieved a 64.2 % clearance rate within 30 min (Fig. 2B).

Catalase (CAT) was integrated into MOF808 through a process that capitalizes on supramolecular interactions, resulting in a sophisticated MOF808@CAT composition. This synergistic assembly significantly bolsters our approach to ROS management, optimizing the clearance of ROS and thereby fortifying the system's antioxidant defenses. As depicted in Fig. 2C, there was a positive correlation between the concentration of MOF808@CAT and the increase in the clearance rate of •OH. In contrast, when MOF808 was applied alone, an inverse effect was observed, highlighting the synergistic contribution of CAT integration to the antioxidant capacity of the composite. Compared with MOF808 at the same concentration, MOF808@CAT demonstrated a significantly greater clearance effect on H_2O_2. Notably, when both were present at a concentration of 2 μg mL^{-1}, the H_2O_2 clearance efficiency of MOF808@CAT was 11.3 times greater than that of MOF808, with percentages of 25 % and 2.1 %, respectively (Fig. 2D). This substantial difference was largely attributed to the CAT-mediated consumption of H_2O_2.

The ESR spectroscopy results revealed that the incorporation of MOF808 and MOF808@CAT, each at a concentration of 200 μg mL^{-1}, significantly attenuated these spectral signals, confirming their ability to scavenge •OH (Fig. 2E). Furthermore, we assessed the $\bullet O_2^-$ quenching potential of these materials via ESR. The addition of MOF808 and MOF808@CAT at a concentration of 200 μg mL^{-1} resulted in a reduction in peak intensity, indicative of their capacity to mitigate $\bullet O_2^-$ (Fig. 2F). We assessed the O_2-generating capabilities of MOF808 and MOF808@CAT via the use of a $[Ru(dpp)_3]Cl_2$ oxygen-sensitive fluorescent probe. MOF808@CAT showed exceptional O_2-generation ability, whereas MOF808 at the same concentration was slightly less effective (Fig. S9). After continuously incubating the probe with the material for 300 s and monitoring its fluorescence intensity, no significant changes in fluorescence intensity were observed over time (Fig. S10). This could be attributed to the fact that MOF808@CAT essentially quenched the fluorescence completely at the initial stage of the reaction by generating O_2. As shown in Fig. 2G, the efficacy of MOF808@CAT in generating O_2 increased with increasing dosage, indicating a dose-dependent effect. Fig. 2H shows a marked reduction in the characteristic absorbance peak of ABTS• cation radicals at 734 nm, which is correlated with increasing concentrations of MOF808@CAT. Fig. S11 presents a quantitative assessment of the ABTS• radical scavenging efficiency. These findings strongly substantiated the superior capacity for anoxic free radical neutralization. These attributes are anticipated to enhance the subsequent antioxidant mechanisms of the material.

3.3. Cytoprotective effects of MOF808 NPs and their cellular uptake by PAC

3.3.1. Cellular uptake and biocompatibility studies in vitro

Primary PAC were isolated according to our previously described experimental methods [14]. The immunofluorescence results confirmed the high expression level of amylases in the acinar cells isolated, which is consistent with the characteristics of PAC (Fig. S12). An H_2O_2-induced oxidative stress cell model was used to simulate acute inflammatory cellular damage. As suggested by the results of the H_2O_2 concentration gradient screening, 200 μM was chosen as the moderate H_2O_2 concentration to establish the oxidative stress model (Fig. S13). After 24 h of coincubation with H_2O_2-induced PAC, FITC-labeled MOF808 and MOF808@BA@CAT were respectively localized with Dil-labeled PAC, indicating the internalization of MOF808 NPs by PAC (Fig. 3A). The CCK-8 assay results indicated no cytotoxicity in PAC exposed to MOF808 NPs at various dosages, with over 80 % of the cells surviving at dosages up to 20 μg mL^{-1} for 24 h (Fig. 3B). Similarly, the biocompatibility of MOF808 NPs was also verified in AR42J cells (Fig. S14). AR42J cells are immortalized pancreatic adenocarcinoma cells that share similarities with normal PAC and are widely used to study the function of the exocrine pancreas. Compared with that of cells damaged by H_2O_2, the viability of inflammatory PAC significantly improved from 40 % to 60 % with coincubation with 10 μg mL^{-1} MOF808 (Fig. 3C). Compared with MOF808 alone, MOF808@BA@CAT demonstrated enhanced

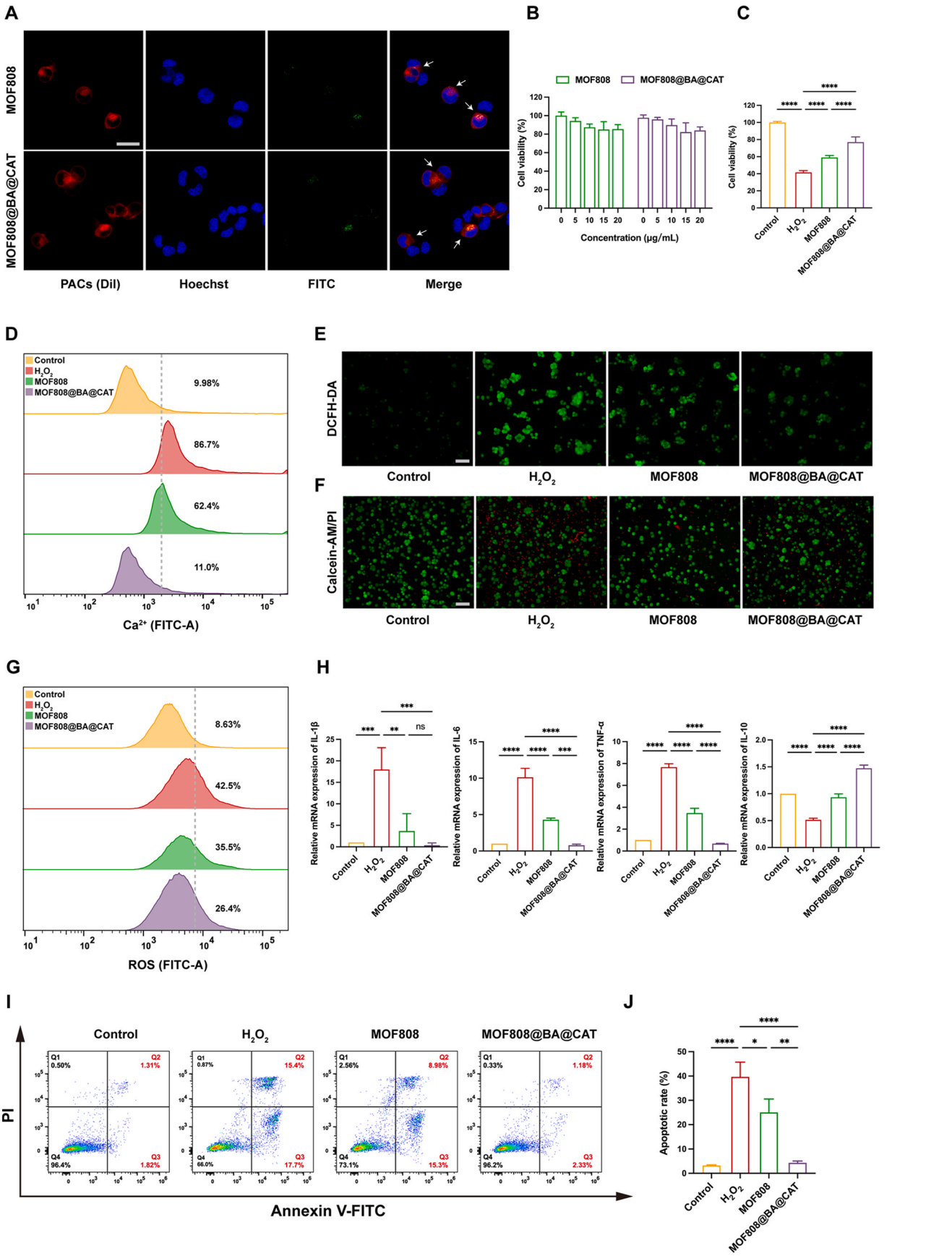

(caption on next page)

Fig. 3. Cellular uptake and protection effects of MOF808 NPs through calcium elimination and ROS scavenging in PACs.
A) Confocal laser scanning microscopy (CLSM) images showed cellular uptake of FITC-labeled MOF808/MOF808@BA@CAT by PACs. Scale bar = 20 μm. B) Viability of PACs treated with different concentrations of MOF808/MOF808@BA@CAT (n = 3). C) Viability of PACs treated with MOF808 NPs followed by H_2O_2 stimulation (n = 3). D) Intracellular calcium levels evaluated in control and H_2O_2-induced PACs with different treatments followed by incubation of the fluo-4 AM probe according to flow cytometry analysis (n = 3). E) Representative fluorescence images of PACs dyed with DCFH-DA under different treatment conditions. Scale bar = 100 μm. F) Representative fluorescence images of PACs dyed with Calcein/AM (green, live cells) and PI (red, dead cells). Scale bar = 100 μm. G) Flow cytometry analysis for ROS production in PACs following different treatments. H) Relative mRNA expression of IL-1β, IL-6, TNF-α and IL-10 in PACs determined by quantitative PCR (n = 3). I, J) Annexin V-fluorescein isothiocyanate (FITC)/PI double staining evaluation of PACs apoptosis and corresponding apoptosis statistics (n = 3). Significant differences between two groups were indicated at $*p < 0.05$, $**p < 0.01$, $***p < 0.001$, and $****p < 0.0001$.

cytoprotective effects, increasing cell viability to approximately 80 %.

3.3.2. Calcium overload elimination in inflammatory PAC

A continuous increase in free cytoplasmic Ca^{2+} ($[Ca^{2+}]_i$) and calcium overload are the primary initial events of PAC injury in almost all types of acute pancreatitis [5]. As shown in Fig. 3D, aberrant calcium overload was detected by flow cytometry in H_2O_2-induced PAC. The MOF808 treatment partially decreased the level of calcium. A superior calcium overload elimination effect was observed in PAC treated with MOF808@BA@CAT, an effect that was partially attributable to the loading of the calcium chelator, which directly binds with intracellular calcium.

3.3.3. ROS scavenging and anti-inflammation ability evaluation

After H_2O_2 stimulation, PAC exhibited intense green fluorescence. MOF808 partially reduced the ROS levels, and MOF808@BA@CAT exhibited better ROS scavenging abilities with faint green fluorescence, which was attributable to the loading of the CAT, which optimized the clearance of ROS (Fig. 3E– S15). The results of flow cytometry indicated that MOF808 reduced the ROS level from 42.5 % to 35.5 %, while MOF808@BA@CAT exhibited enhanced ROS scavenging capacity, reducing the ROS level to 26.4 % (Fig. 3G).

Moreover, the live/dead staining of PAC confirmed the cytoprotective effects of MOF808 NPs (Fig. 3F). In H_2O_2-induced PAC, the ratio of dead/live cells significantly decreased with MOF808 NPs treatment, confirming the excellent cytoprotective effect of MOF808 NPs against oxidative stress damage. After loading with BA and CAT, the cytoprotective effect of MOF808@BA@CAT was significantly enhanced.

The RNA levels of relevant inflammatory cytokine were quantified via real-time quantitative polymerase chain reaction (RT–qPCR). Upon H_2O_2 treatment, PAC presented a significant increase in the RNA levels of proinflammatory cytokines, including IL-1β, IL-6 and TNF-α, with a decrease in the mRNA level of the anti-inflammatory cytokine IL-10. The presence of MOF808 NPs inhibited the secretion of proinflammatory cytokines while increasing the secretion of the anti-inflammatory cytokine IL-10, indicating the ability of MOF808 NPs to reduce the degree of cellular inflammation. MOF808@BA@CAT exhibited better anti-inflammatory effects than did MOF808 (Fig. 3H). Moreover, the secretion levels of IL-1β, IL-6, IL-10 and TNF-α from PAC under different treatment were detected via Elisa assay, and the results also confirmed the enhanced anti-inflammatory effect of MOF808@BA@CAT (Fig. S16).

Excessive ROS generation can lead to cell apoptosis. The introduction of MOF808 NPs noticeably decreased the proportion of apoptotic cells induced by H_2O_2, providing evidence of their cytoprotective properties. After loading with BA and CAT, MOF808@BA@CAT exhibited stronger antiapoptotic properties and reduced the proportion of apoptotic cells to close to that of the control group (Fig. 3I and J).

3.4. Restoration of mitochondrial dysfunction

Mitochondria serve as cellular power sources and are the primary intracellular producers of ROS [32]. Excess superoxide will lead to mitochondrial oxidative stress damage and dysfunction, which in turn leads to pathologies such as cell death. The Mito Sox Red fluorescent probe was used to assess mitochondrial superoxide levels. The mitochondria subjected to H_2O_2-induced damage presented a robust red fluorescent signal (Fig. 4A and B). MOF808@BA@CAT treatment led to an obvious reduction in the fluorescent signal, which indicated the protective effect of MOF808 NPs on mitochondria under inflammation.

The mitochondria in healthy cells exhibit a filamentous mitochondrial network. CypD (Cyclophilin D) can lead to the formation and opening of a tunable MPTP through Ca^{2+} signaling [33,34]. The mitochondria of H_2O_2-induced PAC presented a fragmented structural appearance, with increased expression levels of CypD (Fig. 4C). MOF808 treatment led to a reduction in the CypD fluorescence signal and partial restoration of the mitochondrial structure. In contrast, treatment with MOF808@BA@CAT resulted in an obvious tendency toward the restoration of the typical filamentous mitochondrial structure and simultaneously lower expression of CypD. Western blot results also confirmed that MOF808@BA@CAT treatment reduced the high expression level of CypD in H_2O_2-induced PAC (Fig. 4D– S17). Moreover, after incubation with MOF808@BA@CAT, the impaired mitochondrial autophagy in H_2O_2-induced PAC was ameliorated, which was confirmed by western blot analysis of components of the Beclin1/p62/LC3A/B pathway (Fig. 4D– S17).

The opening of the MPTP can further cause a decrease in the mitochondrial membrane potential (Δψm), a hallmark of apoptotic cell death, with a consequent reduction in mitochondrial ATP production. The addition of MOF808 NPs increased the production of ATP, as shown by ATP assay kit detection (Fig. 4E). To assess the effect of MOF808 NPs on the mitochondrial membrane potential, PAC in each experimental group were stained with JC-1. JC-1 accumulates and forms aggregates in the mitochondrial matrix of cells with a high mitochondrial membrane potential, resulting in intense red fluorescence. CLSM revealed that following H_2O_2 stimulation, the red fluorescence decreased, whereas the green fluorescence increased, indicating a decrease in the mitochondrial membrane potential. The addition of MOF808 NPs significantly attenuated the decrease in the mitochondrial membrane potential, while the changes in the MOF808@BA@CAT group were remarkably more pronounced than those in the MOF808 group (Fig. 4F and G). Furthermore, flow cytometry analysis confirmed the maintenance effect of MOF808@BA@CAT on the mitochondrial membrane potential (Fig. 4H and I).

3.5. Anti-inflammatory and antioxidant effects of MOF808 NPs in vivo

First, to assess the long-term biosafety of MOF808 NPs, we measured the changes in serum biochemical indicators and main organs in healthy rats after one month of high-dose treatment (2 mg kg^{-1}). Serum biochemistry indices and histopathology of the main organs after MOF808 NPs administration revealed no observable impairments (Figs. S18 and 19). These results preliminarily indicated that MOF808 NPs have reliable biosafety.

An SAP model was constructed by retrograde biliopancreatic duct injection of 3 % NaT as previously described in our study (Fig. 5A) [14, 35,36]. MOF808 NPs were injected into SAP rats via the tail vein 6 h after the induction of SAP. Pancreas, lung, and serum samples were extracted 48 h after treatment for subsequent detection (Fig. 5B). Compared with those in the sham group, the pancreatic tissue in the SAP group showed massive necrosis and edema. After MOF808 (1.5 mg kg^{-1}) and MOF808@BA@CAT (1.5 mg kg^{-1}) treatment, the pancreatic tissue

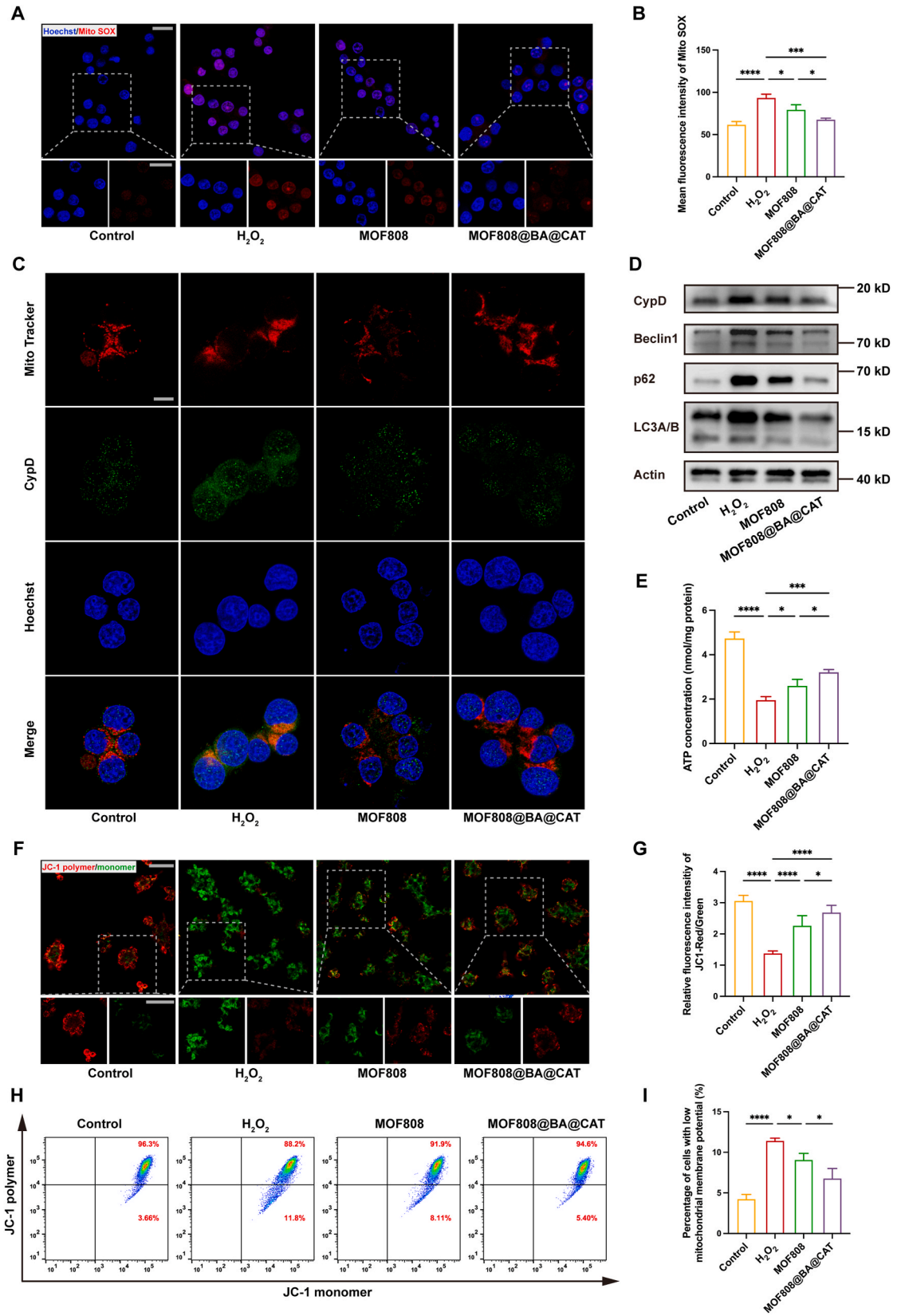

Fig. 4. Improvement of mitochondrial dysfunction by MOF808 NPs.
A, B) Representative CLSM images of mitochondrial ROS levels in PACs detected by the Mito Sox fluorescent probe. Scale bar = 20 μm. C) Representative images of mitochondrial morphology changes detected by Mito Tracker and CypD expression detected by immunofluorescence. Scale bar = 10 μm. D) Western blot analysis of CypD, Beclin1, p62 and LC3A/B. E) Expression levels of ATP in PACs from different treatment groups (n = 3). F, G) Representative images of JC-1 fluorescence staining was analyzed by confocal microscopy. Scale bar = 50 μm. H, I) Flow cytometry analysis of mitochondrial membrane potential using JC-1 fluorescence. *$p < 0.05$, **$p < 0.01$, ***$p < 0.001$, and ****$p < 0.0001$.

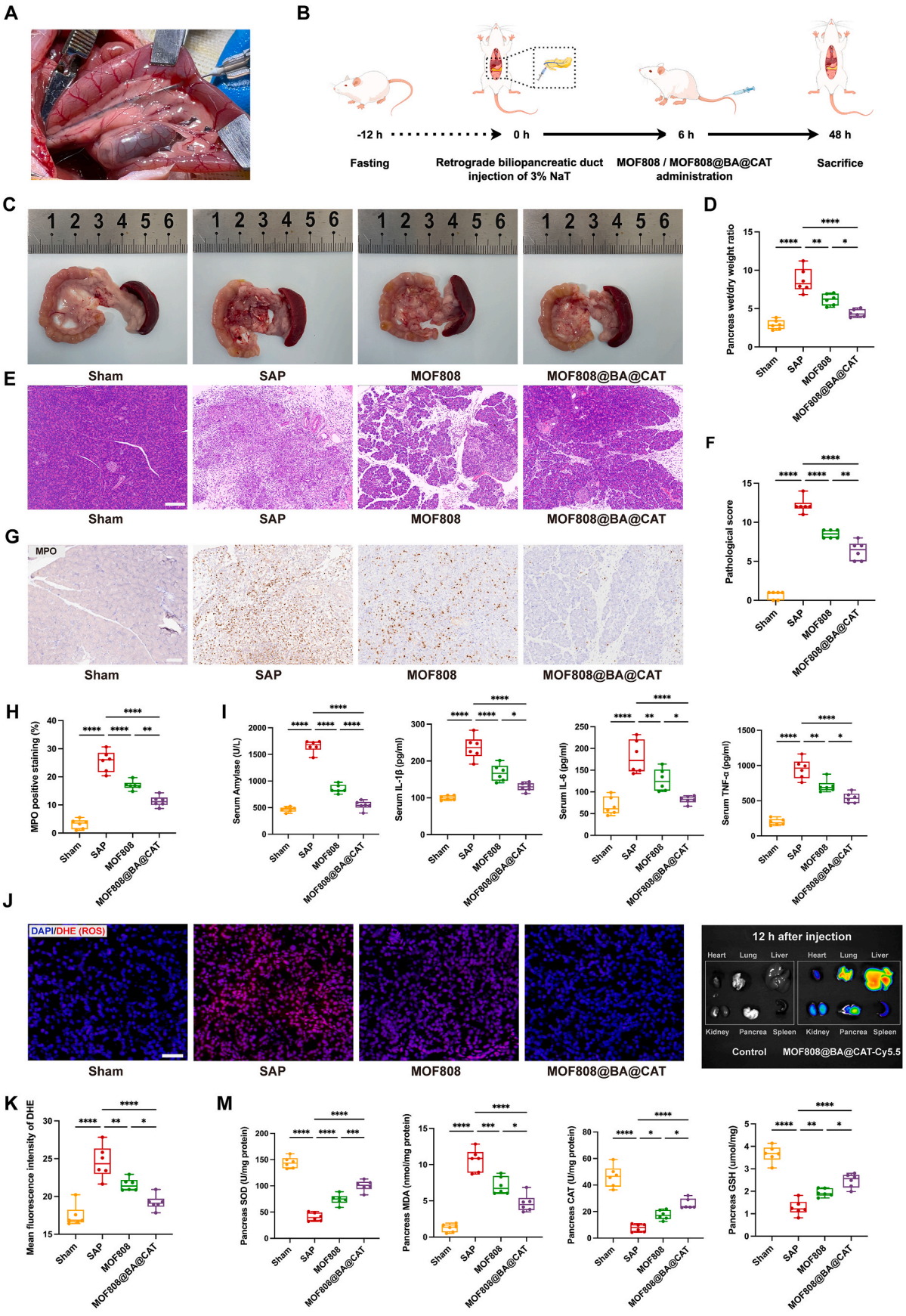

(caption on next page)

Fig. 5. Anti-inflammatory and antioxidant effects of MOF808 NPs in vivo.
A) Retrograde biliopancreatic duct injection of 3 % NaT to established the SAP model. B) Schematic diagram of vivo experiments (Created by Figdraw). C) Representative images of pancreatic tissue and D) pancreas wet/dry weight ratio of each group (n = 6). E) Pancreas slices stained with Hematoxylin and eosin (H&E). Scale bar = 200 μm. F) Pathological scores for H&E staining in the pancreas. G, H) Immunohistochemical staining of pancreatic tissue for the neutrophil marker myeloperoxidase (MPO). Scale bar = 100 μm. I) The level of amylase, IL-1β, IL-6 and TNF-α in the serum. J, K) Representative images of dihydroethidium (DHE) staining in pancreatic tissue. Scale bar = 50 μm. L) In vivo fluorescence imaging of Cy5.5-labeled MOF808@BA@CAT showed an accumulation in main organs (liver, lung, spleen, pancreas, kidney and heart) 12 h after intravenous injection. M) The level of SOD, MDA, CAT and GSH in the pancreas. $^{*}p < 0.05$, $^{**}p < 0.01$, $^{***}p < 0.001$, and $^{****}p < 0.0001$.

histomorphology significantly improved, with reduced areas of necrosis and edema and lower wet/dry weight ratios (Fig. 5C and D). Correspondingly, hematoxylin and eosin (H&E) staining of pancreatic tissues revealed that MOF808 injection decreased the pathological score, an effect that was more obvious in the MOF808@BA@CAT group (Fig. 5E and F). Moreover, SAP-related acute lung injury was effectively alleviated after treatment with MOF808@BA@CAT, as shown by H&E staining (Fig. S20). The pancreatic tissue of the SAP rats treated with MOF808@BA@CAT exhibited less neutrophil infiltration (Fig. 5G and H) and cytoplasmic release of HMGB1 (Fig. S21), a prototype damage-associated molecular pattern (DAMP) released by injured cells. Furthermore, compared with MOF808, MOF808@BA@CAT inhibited the level of systemic inflammation more significantly, with decreased levels of serum amylase and proinflammatory cytokines (IL-1β, IL-6, and TNF-α) (Fig. 5I). These results provide evidence for the effective mitigation of systemic inflammation in SAP rats through the administration of MOF808@BA@CAT.

During SAP progression, large quantities of oxygen free radicals are produced, accompanied by oxidative stress injury. After MOF808 treatment, the ROS level in pancreatic tissue significantly decreased, while MOF808@BA@CAT exhibited greater ROS scavenging capacity (Fig. 5J and K). As a consequence of lipid peroxidation, products of lipid peroxidation (MDA) are released. SOD, the primary enzyme in the antioxidant enzyme defense system, can halt the free radical chain reaction, leading to lipid peroxidation and protecting cells and tissues from ROS damage. The administration of MOF808 significantly decreased the level of MDA while promoting SOD, CAT and GSH activity. Moreover, the enhanced antioxidative ability was observed in rats treated with MOF808@BA@CAT (Fig. 5M).

To investigate the potential migration of MOF808@CAT@BA to the pancreas via the blood circulation for therapeutic purposes, we labeled it with Cy5.5 dye and administered it intravenously through the tail vein. The fluorescence signal distribution in rats was subsequently monitored at various time intervals. MOF808@BA@CAT was detected in the main organs 12 h after injection and was still detected in the pancreatic tissue after 48 h (Fig. 5L– S22). In addition, the detectable levels of cerium in the pancreatic tissue were confirmed by ICP-MS elemental analysis (Fig. S23). These results demonstrated that MOF808@BA@CAT clearly suppressed inflammation and oxidative stress in the pancreatic tissues of SAP rats.

3.6. Restoration of mitochondrial dysfunction in SAP rats

Severe inflammation impacts the mitochondrial antioxidant system of PAC and increases their susceptibility to oxidative damage. Transmission electron microscopy (TEM) was used to observe the mitochondrial morphology of acinar cells in pancreatic tissues (Fig. 6A). Mitochondrial ridge shrinkage, mitochondrial swelling and vacuolization were observed in SAP model rats. After MOF808 treatment, the mitochondria partially recovered their oval shape, whereas MOF808@BA@CAT enhanced their ability to restore mitochondria.

TOM20, a mitochondrial protein, is readily degraded in response to oxidative stress [37], which is consistent with our immunofluorescence results in the SAP group (Fig. 6B). The pancreas of SAP rats treated with MOF808@BA@CAT exhibited significant recovery of TOM20 expression, indicating the high protective efficacy of MOF808@BA@CAT for mitochondria (Fig. 6B). Similarly, both western blot and immunofluorescence confirmed that CypD was highly expressed under oxidative stress, and was effectively reduced after MOF808@BA@CAT administration (Fig. 6C, D, S24). Western blot analyses were performed to determine the protein expression of autophagy pathway markers (Beclin1/p62/LC3A/B). Compare with SAP, MOF808@BA@CAT significantly decreased the expression of markers in autophagy pathways (Fig. 6D– S24). Moreover, given that endoplasmic reticulum stress (ER stress) is also a key pathogenic process affecting acinar cell functions [8], the expression of associated proteins (ATF6, GRP78 and CHOP) in pancreatic tissues was assessed. MOF808@BA@CAT clearly reversed the overexpression of ER stress-related proteins (Fig. 6E– S24).

3.7. Therapeutic mechanism of MOF808@BA@CAT on SAP

3.7.1. Metabolomic analysis

To elucidate the therapeutic mechanism of MOF808@BA@CAT in SAP, untargeted metabolomic analysis of the pancreatic tissues of rats was performed (Fig. 7A). A total of 1105 metabolites were identified via LC−MS analytical techniques and data processing methods. Principal component analysis (PCA) of the data revealed significant variations in the distribution of metabolites among the sham group, SAP group, and MOF808@BA@CAT groups (Fig. S25). Volcano plots revealed that 106 metabolites were increased and 25 metabolites were decreased in SAP rats compared with sham rats, whereas 36 metabolites were increased and 44 metabolites were decreased after MOF808@BA@CAT treatment (Fig. 7B); among the increased and decreased metabolites, 29 metabolites and 3 metabolites overlapped between those two sets of comparisons, respectively, which could be related to the MOF808@BA@CAT treatment (Fig. 7C). The metabolites whose abundance decreased before and after MOF808@BA@CAT treatment were then selected to construct a heatmap (Fig. 7D). After MOF808@BA@CAT treatment, the metabolites whose abundance was altered in SAP mostly returned to an abundance similar to that of the control group, which suggested that MOF808@BA@CAT may alleviate inflammation by reversing abnormal metabolism in SAP. These differentially abundant metabolites were further analyzed via enrichment and pathway analyses via the Kyoto Encyclopedia of Genes and Genomes (KEGG) database. Pathway analysis revealed that the most differentially abundant metabolites before and after MOF808@BA@CAT treatment were related to alanine, aspartate and glutamate metabolism; vitamin B6 metabolism; purine metabolism; and glutathione metabolism (Fig. 7E). Gene set enrichment analysis (GSEA) revealed that most of the metabolites were negatively correlated with bile secretion in SAP but were positively correlated after MOF808@BA@CAT treatment, with enrichment scores of −0.64 and 0.65, respectively (Fig. 7F). The altered correlation of metabolites indicated that pancreatic duct function tended to normalize after MOF808@BA@CAT treatment, thus allowing smooth drainage of bile and pancreatic fluid into the intestine and preventing the aggravation of SAP due to obstruction by pancreatic duct injury.

3.7.2. RNA sequencing analysis of MOF808@BA@CAT in PAC

RNA sequencing analysis of primary PAC was performed to elucidate the molecular mechanisms of MOF808@BA@CAT treatment. PCA revealed significant variations in the distribution (Fig. S26). Differentially expressed gene (DEG) analysis revealed that a total of 1581 genes were upregulated and 1613 genes were downregulated in the H_2O_2-induced group compared with the control group, whereas 720 DEGs

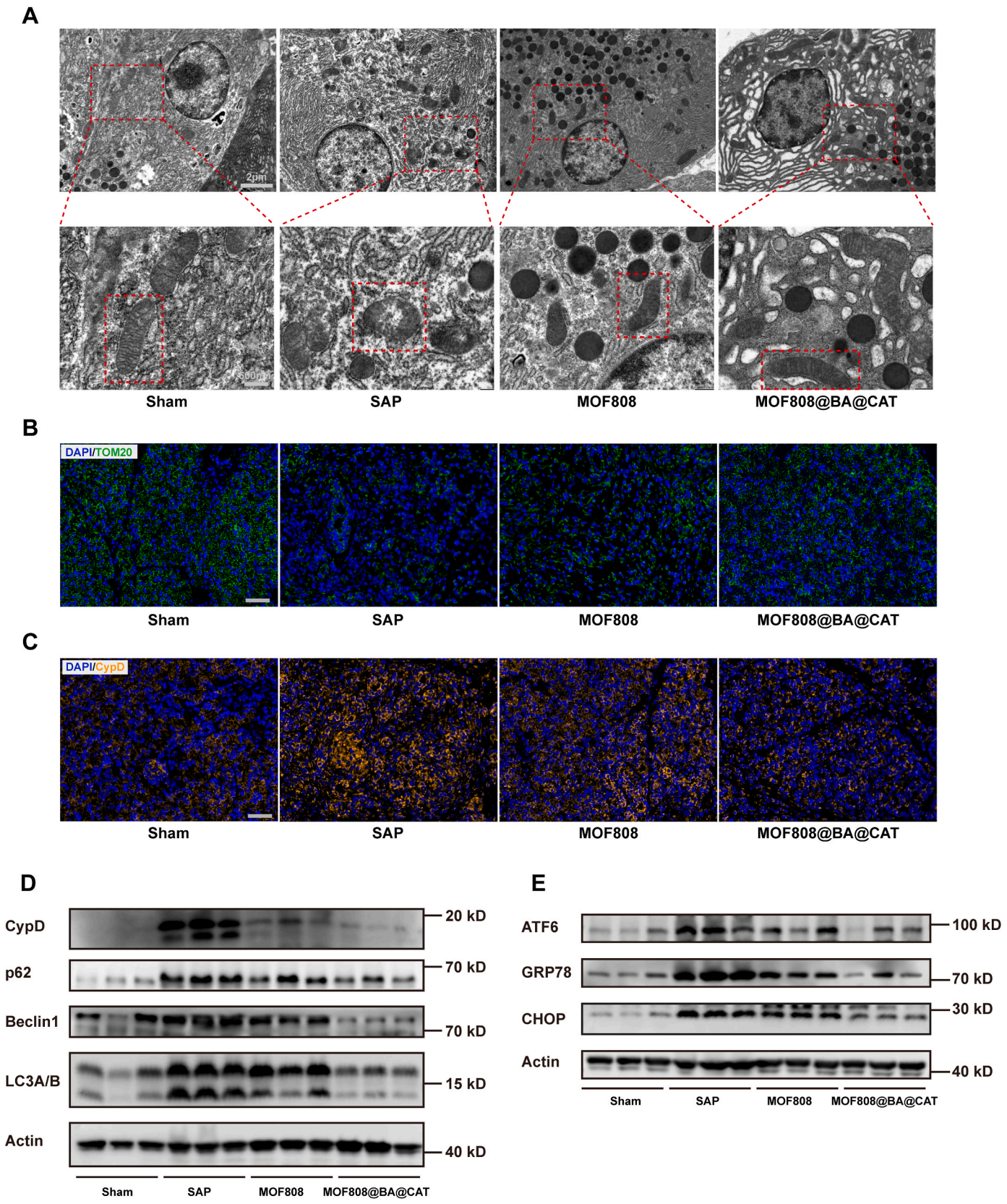

Fig. 6. Restoration of mitochondrial damage in pancreatic tissue by MOF808 NPs.
A) TEM images of mitochondrial morphology in pancreatic tissue. (Representative mitochondrial images were shown in red boxes). B) Immunofluorescence assay of TOM20 and C) CypD expression levels in pancreatic tissues. Scale bar = 50 μm. D) CypD, markers in autophagy pathways and E) endoplasmic reticulum (ER) stress in pancreatic tissue were analyzed by Western blot.

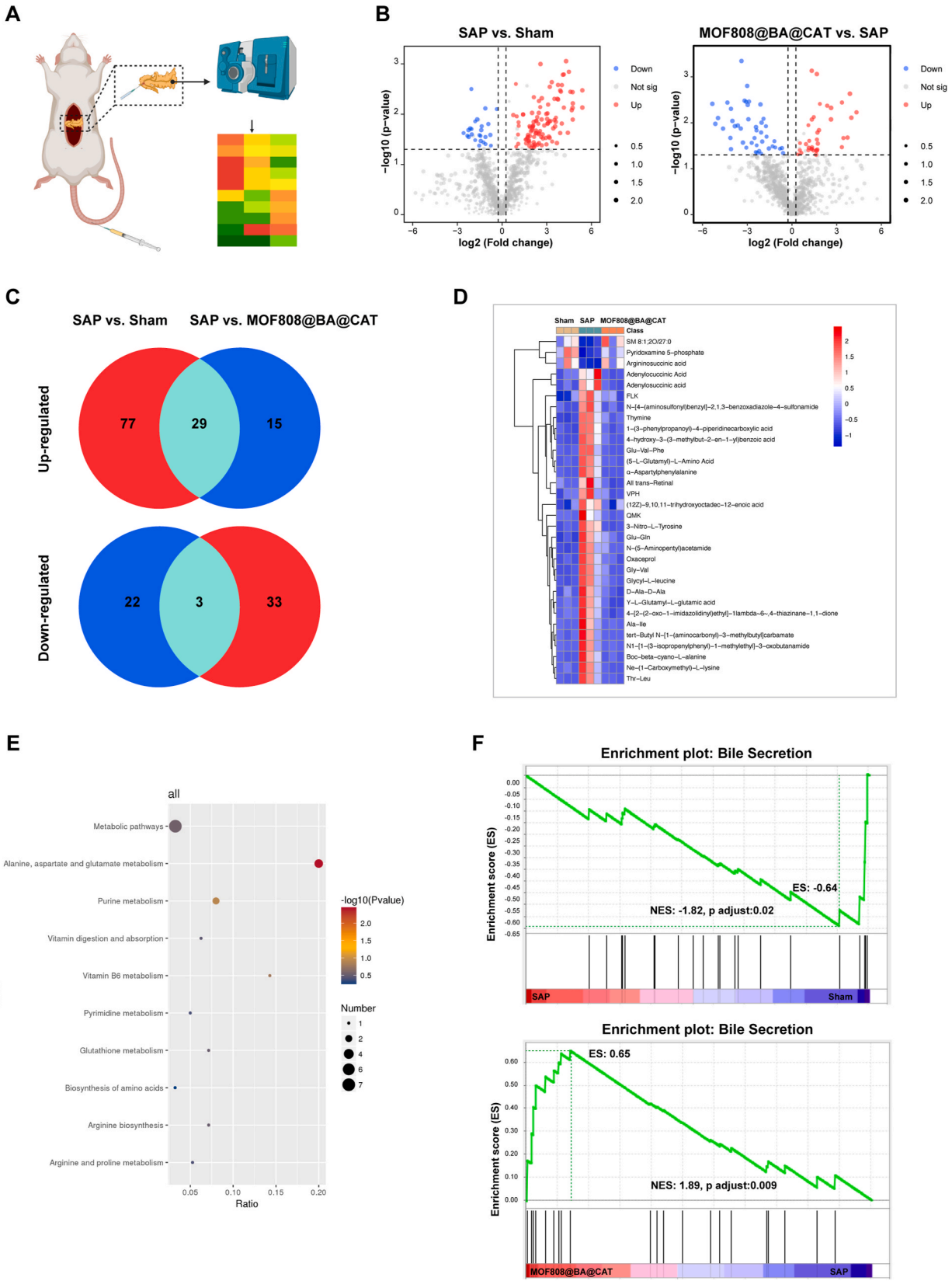

Fig. 7. The reversal metabolic abnormalities in pancreatic tissue after MOF808@BA@CAT treatment.
A) Schematic diagram of metabolome sequencing. B) Volcano plots for differential expression analysis of identified metabolites. C) Venn diagram revealed overlapping differential metabolites of each group. D) Heatmap showed the reversal abundance of differential metabolites after MOF808@BA@CAT treatment. E) Enrichment analysis of reversal metabolites in the pancreas. F) GSEA enrichment maps of differential metabolites focused on regulation of bile secretion.

(352 upregulated and 370 downregulated) were identified between the MOF808@BA@CAT group and the H_2O_2-induced PAC (Fig. 8A); among the upregulated and downregulated DEGs, 280 and 290 DEGs overlapped between those two sets of comparisons, respectively (Fig. 8B). KEGG enrichment analysis revealed that MOF808@BA@CAT downregulated genes enriched in various regulatory pathways, including the "pancreatic secretion", "TNF signaling", "IL-17 signaling", and "NF-kappa B signaling" pathways (Fig. 8C). These results suggested that MOF808@BA@CAT treatment suppressed inflammation-related pathways, which are closely related to the progression of SAP, particularly the NF-kappa B signaling pathway. Moreover, Gene Ontology (GO) enrichment analysis was performed to identify the biological process, cellular component and molecular function associated with the downregulated DEGs (Fig. 8D). In particular, the main enriched GO terms of the biological process category included "intrinsic apoptotic signaling pathway", "response to reactive oxygen species", "acute inflammation response" and "apoptotic mitochondrial changes". Moreover, a total of 7 modules were revealed via weighted gene coexpression network analysis (WGCNA), which revealed significant changes in gene associations after MOF808@BA@CAT treatment (Fig. 8E). For example, the MEblue module and the MEyellow module were positively correlated with the H_2O_2 group but not with the MOF808@BA@CAT treatment group. The genes involved in the MEblue module were selected for further GO and KEGG analysis via Cytoscape (version 3.7.0) to construct an enrichment network (Fig. 8F). The results revealed that the majority of the gene clusters were enriched in mitochondria, the endomembrane system, the apoptotic process, the proteasome, and cellular component assembly, which indicated that MOF808@BA@CAT may alleviate inflammation by affecting these related genes.

The sequencing results provide insights into the molecular mechanisms underlying the anti-inflammatory effects of MOF808@BA@CAT from the perspective of altered signaling pathways and provide further evidence for the therapeutic effects of this nanoplatform against SAP.

4. Discussion

SAP is characterized by severe pancreatic inflammation and considerable acinar cell damage, accompanied by a fast and systemic inflammatory response, resulting in organ dysfunction lasting more than 48 h [1]. Owing to the rapid changes and complex progress during SAP, conventional treatment has limited efficacy and a poor prognosis. Our group has extensively explored new strategies for treating SAP, such as mesenchymal stem cell (MSC) therapy [14,38,39] and MSC-derived extracellular vesicle therapy [35,36]. Despite the sufficient exploration performed by our group, relevant clinical research on the treatment of SAP has not yet been effectively conducted due to the risk of potential immunogenicity. Therefore, there is an urgent need to explore new strategies or potential drugs for treating SAP to prevent progression efficiently and relieve pancreatic damage.

The initial critical events in pancreatic injury involve abnormally high levels of intracellular calcium and the premature and massive activation of digestive enzymes in acinar cells, resulting in the pathological autodigestion of acinar cells. The excessive generation of ROS, caused by the stimulation of various pathological factors, leads to oxidative stress. Mitochondria, a prominent source of ROS, are also susceptible to calcium overload. These pathological signals cause abnormal opening of the MPTP, resulting in mitochondrial dysfunction. The impairment of mitochondrial function due to abnormal MPTP opening is a critical event in all studied types of acute pancreatitis [9,40]. The resulting amplified cascade of events, including reduced ATP production, impaired autophagy, and cytokine release, culminates in an increasingly intense inflammatory response that ultimately leads to pancreatic necrosis. Most previous studies have focused on therapeutic targets for inhibiting the abnormal opening of MPTPs [41]. Despite impressive results in animal studies, improving severe pancreatic necrosis via this treatment alone is difficult because the progression of SAP-related inflammation is exacerbated not only by the abnormal opening of MPTPs but also by calcium overload and excessive ROS production.

In recent years, biomedicine has gained extensive attention as a strategy for treating and managing various inflammatory diseases, as well as monitoring during treatment [23,24,42,43]. In pancreatic related diseases, the previous study reported that excipient-free self--assembled nanotheranostics exerted significant anticancer effects in a mouse model of pancreatic cancer [44]. In diabetes-related studies, the antioxidative nanozymes properties could scavenge diabetes-induced ROS, resulting in macrophage polarization towards the anti-inflammatory phenotype [45]. Hosseini et al. demonstrated anti-apoptotic activity of cerium nanoparticles in oxidative stress induced apoptosis of pancreatic islets in response to H_2O_2, this cerium nanoparticles may protect β-cell apoptosis by improving the oxidative stress-mediated apoptotic pathway [20]. Therefore, cerium nanoparticle is a promising strategy with multiple possibilities for pancreatic related diseases.

In our study, we constructed a unique anti-inflammatory nanoplatform, MOF808@BA@CAT, by binding BAPTA-AM to achieve calcium elimination and loading of CAT to achieve enhanced ROS scavenging capacity. As a proof of concept, in a classical and clinically relevant biliary SAP rat model, we revealed that the constructed nanoplatform (MOF808@BA@CAT) efficiently inhibited oxidative stress and systematic inflammation, alleviating pancreatic lesions. The pharmacodynamic results revealed that a single dose of the as-prepared formulation (1.5 mg kg^{-1}) alleviated pancreatic injury and significantly decreased the serum amylase and proinflammatory cytokine levels. The results of in vitro experiments revealed that MOF808@BA@CAT demonstrated a significant Ca^{2+} reduction ability after encapsulating the hydrophobic drug BAPTA-AM. After incubation with MOF808@BA@CAT, mitochondrial dysfunction in damaged PAC was improved, and the CypD-mediated opening of MPTPs was alleviated. Moreover, enhanced ROS scavenging ability was also demonstrated in injured PAC. MOF808@BA@CAT exerts a key therapeutic effect by eliminating calcium and alleviating oxidative stress and mitochondrial dysfunction.

Moreover, MOF808@BA@CAT administration reversed the abnormal metabolite levels in SAP pancreatic tissue. Consistent with previous studies, amino acid metabolism pathways such as alanine, aspartate and glutamate metabolism, and arginine and proline metabolism are abnormally active in SAP rats, which is attributed to the fact that when pancreatic acinar cells are stimulated by damage, the stimulus could cause metabolic disequilibrium through activation of calcium and generation of excess reactive oxygen species leading to mitochondrial injury and thus metabolic disorders, and the disrupted metabolites might in turn further induce oxidative stress [46,47]. In addition, MOF808@BA@CAT administration enhanced bile secretion to prevent the aggravation of SAP due to obstruction by pancreatic duct injury. These abnormal metabolism pathways were partially reversed after MOF808@BA@CAT treatment, and we propose that MOF808 and CAT are able to rescue the metabolic disequilibrium by directly inhibiting oxidative stress and possibly the activity of related metabolic enzymes. Meanwhile, BA is able to chelate Ca^{2+} directly and block the related metabolic disorders by inhibiting calcium over-activation to prevent mitochondrial injury. Transcriptome sequencing of PAC also confirmed that MOF808@BA@CAT administration inhibited inflammation-related signaling pathways, such as the TNF signaling pathway, the NF-κB signaling pathway, and the apoptotic signaling pathway.

5. Conclusion

In conclusion, we successfully developed an effective strategy for the treatment of SAP based on nanoparticles. The powerful anti-inflammatory and antioxidative stress effects of MOF808@BA@CAT significantly alleviated severe damage of the pancreas. However, it remains to be clarified whether MOF NPs can improve systemic

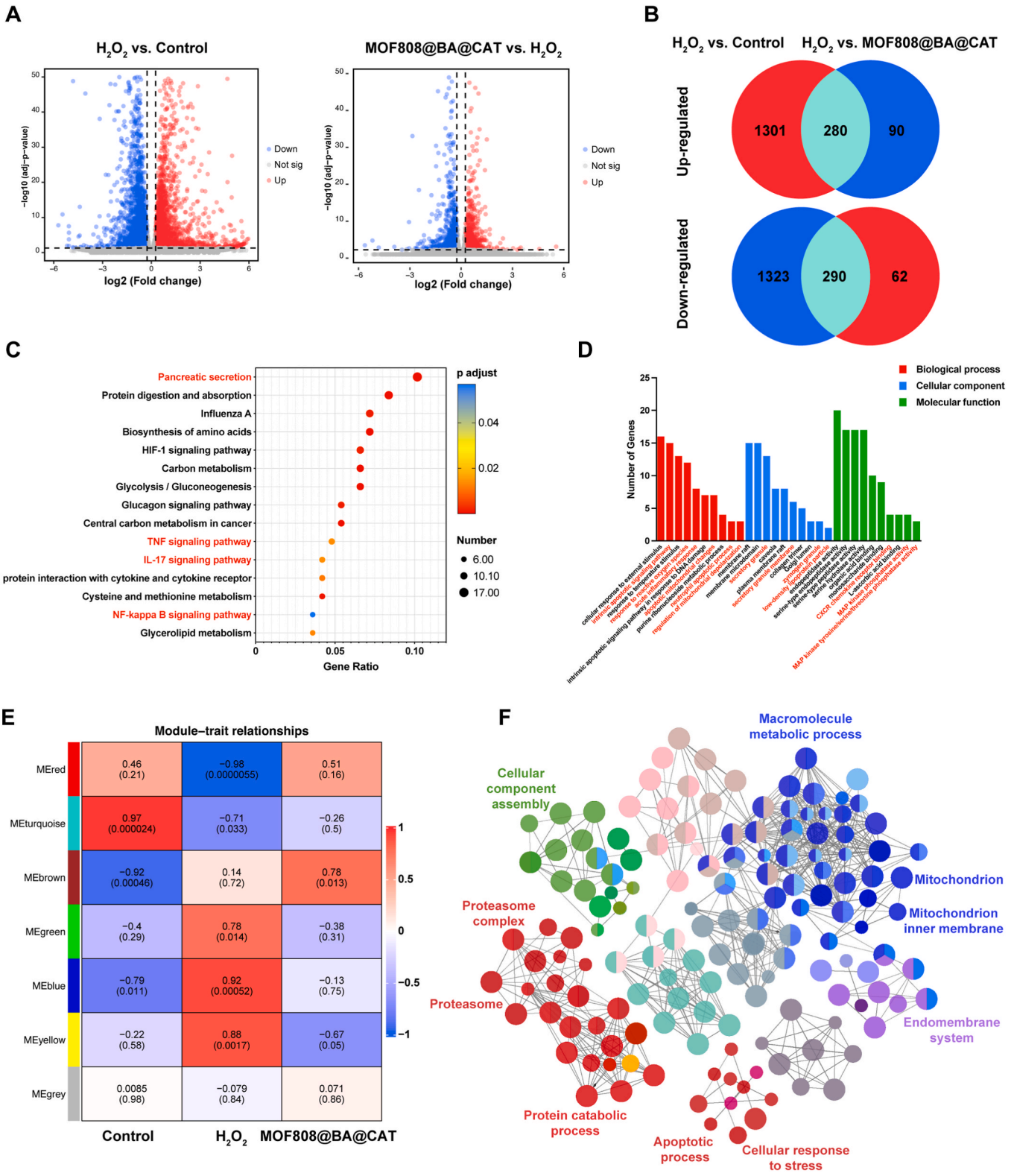

Fig. 8. RNA sequencing analysis of PACs treated with MOF808@BA@CAT.
A) Volcano plots for differentially expressed genes (DEGs) of each group. B) Venn diagram showed overlapping DEGs of each group. C) Kyoto Encyclopedia of Genes and Genomes (KEGG) enrichment analysis demonstrated primary enrichment pathway of overlapping DEGs. D) Gene ontology (GO) enrichment analysis of overlapping DEGs in the category of biological process, cellular component, and molecular function analysis. E) Module-trait heatmap of the correlation for the three groups identified through weighted gene co-expression network analysis (WGCNA). Each module contains the corresponding correlation coefficient and p value. F) GO and KEGG analysis of the genes involved in the MEblue module.

complications caused by SAP. It is also well worth investigating whether MOF can improve the pancreatic endocrine and exocrine dysfunction left after recovery from SAP. While the present study offers promising outcomes, the applicability of this nanoplatform to clinical settings still requires further exploration. Future studies will focus on assessing the long-term biocompatibility of this nanoplatform to confirm its safety and efficacy in SAP patients. In short, this research demonstrated that MOF808@BA@CAT has great potential for improving SAP outcomes, thus providing a foundation for the development of new strategies for SAP treatment based on nanozymes.

CRediT authorship contribution statement

Tingyi Luo: Writing – original draft, Project administration, Conceptualization. **Yujing Tang:** Writing – original draft, Validation, Methodology. **Wangcheng Xie:** Validation, Formal analysis, Data curation. **Zhilong Ma:** Funding acquisition, Formal analysis. **Jian Gong:** Supervision, Investigation. **Yonggui Zhang:** Project administration. **Tingsong Yang:** Resources, Methodology. **Xuyang Jia:** Visualization. **Jia Zhou:** Supervision. **Zhengyu Hu:** Methodology, Investigation. **Lin Han:** Writing – review & editing. **Qigang Wang:** Writing – review & editing, Funding acquisition, Conceptualization. **Zhenshun Song:** Writing – review & editing, Methodology, Funding acquisition, Conceptualization.

Declaration of competing interest

The authors declare that they have no known competing financial interests or personal relationships that could have appeared to influence the work reported in this paper.

Acknowledgements

Tingyi Luo, Yujing Tang, and Wangcheng Xie contributed equally to this work. This work was supported by the grant from Shanghai Fourth People's Hospital Discipline Construction Project (SY-XKZT-2022-1001; sykyqd05401), the National Science Fund for Distinguished Young Scholars (No. 52125305), the National Natural Science Foundation of China (No. 82200717) and the Changning District medical and health research project (CNKW 2024Y17). The authors thank Home for Researchers (www.home-for-researchers.com) for assistance in creating the schematic diagram.

Appendix A. Supplementary data

Supplementary data to this article can be found online at https://doi.org/10.1016/j.mtbio.2025.101489.

Data availability

Data will be made available on request.

References

[1] S.G. Barreto, A. Habtezion, A. Gukovskaya, A. Lugea, C. Jeon, D. Yadav, P. Hegyi, V. Venglovecz, R. Sutton, S.J. Pandol, Critical thresholds: key to unlocking the door to the prevention and specific treatments for acute pancreatitis, Gut 70 (2021) 194–203, https://doi.org/10.1136/gutjnl-2020-322163.
[2] M.A. Mederos, H.A. Reber, M.D. Girgis, Acute pancreatitis: a review, JAMA 325 (2021) 382–390, https://doi.org/10.1001/jama.2020.20317.
[3] L. Boxhoorn, R.P. Voermans, S.A. Bouwense, M.J. Bruno, R.C. Verdonk, M. A. Boermeester, H.C. van Santvoort, M.G. Besselink, Acute pancreatitis, Lancet 396 (2020) 726–734, https://doi.org/10.1016/S0140-6736(20)31310-6.
[4] O.J. Hines, S.J. Pandol, Management of severe acute pancreatitis, BMJ 367 (2019) l6227, https://doi.org/10.1136/bmj.l6227.
[5] P.J. Lee, G.L. Papachristou, New insights into acute pancreatitis, Nat Rev Gastro Hepat 16 (2019) 479–496, https://doi.org/10.1038/s41575-019-0158-2.
[6] J. Mayerle, M. Sendler, E. Hegyi, G. Beyer, M.M. Lerch, M. Sahin-Toth, Genetics, cell biology, and pathophysiology of pancreatitis, Gastroenterology 156 (2019), https://doi.org/10.1053/j.gastro.2018.11.081, 1951-1968 e1951.
[7] D.N. Criddle, Reactive oxygen species, Ca(2+) stores and acute pancreatitis; a step closer to therapy? Cell Calcium 60 (2016) 180–189, https://doi.org/10.1016/j.ceca.2016.04.007.
[8] G. Biczo, E.T. Vegh, N. Shalbueva, O.A. Mareninova, J. Elperin, E. Lotshaw, S. Gretler, A. Lugea, S.R. Malla, D. Dawson, P. Ruchala, J. Whitelegge, S.W. French, L. Wen, S.Z. Husain, F.S. Gorelick, P. Hegyi, Z. Rakonczay Jr., I. Gukovsky, A. S. Gukovskaya, Mitochondrial dysfunction, through impaired autophagy, leads to endoplasmic reticulum stress, deregulated lipid metabolism, and pancreatitis in animal models, Gastroenterology 154 (2018) 689–703, https://doi.org/10.1053/j.gastro.2017.10.012.
[9] R. Mukherjee, O.A. Mareninova, I.V. Odinokova, W. Huang, J. Murphy, M. Chvanov, M.A. Javed, L. Wen, D.M. Booth, M.C. Cane, M. Awais, B. Gavillet, R. M. Pruss, S. Schaller, J.D. Molkentin, A.V. Tepikin, O.H. Petersen, S.J. Pandol, I. Gukovsky, D.N. Criddle, A.S. Gukovskaya, R. Sutton, N.P.B.R. Unit, Mechanism of mitochondrial permeability transition pore induction and damage in the pancreas: inhibition prevents acute pancreatitis by protecting production of ATP, Gut 65 (2016) 1333–1346, https://doi.org/10.1136/gutjnl-2014-308553.
[10] A. Jakkampudi, R. Jangala, B.R. Reddy, S. Mitnala, D. Nageshwar Reddy, R. Talukdar, NF-kappaB in acute pancreatitis: mechanisms and therapeutic potential, Pancreatology 16 (2016) 477–488, https://doi.org/10.1016/j.pan.2016.05.001.
[11] J. Maleth, P. Hegyi, Ca2+ toxicity and mitochondrial damage in acute pancreatitis: translational overview, Philos. Trans. R. Soc. Lond. B Biol. Sci. 371 (2016), https://doi.org/10.1098/rstb.2015.0425.
[12] W. Zhu, S. Takeuchi, S. Imai, T. Terada, T. Ueda, Y. Nasu, T. Terai, R.E. Campbell, Chemigenetic indicators based on synthetic chelators and green fluorescent protein, Nat. Chem. Biol. 19 (2023) 38–44, https://doi.org/10.1038/s41589-022-01134-z.
[13] Z. Fu, D. Wang, C. Zheng, M. Xie, Y. Chen, Y. Zhou, Y. Huang, Y. Song, W. Hong, Elimination of intracellular Ca(2+) overload by BAPTA-AM liposome nanoparticles: a promising treatment for acute pancreatitis, Int. J. Mol. Med. 53 (2024), https://doi.org/10.3892/ijmm.2024.5358.
[14] Z. Hu, D. Wang, J. Gong, Y. Li, Z. Ma, T. Luo, X. Jia, Y. Shi, Z. Song, MSCs deliver hypoxia-treated mitochondria reprogramming acinar metabolism to alleviate severe acute pancreatitis injury, Adv. Sci. 10 (2023) e2207691, https://doi.org/10.1002/advs.202207691.
[15] C. Zhang, X. Wang, J. Du, Z. Gu, Y. Zhao, Reactive oxygen species-regulating strategies based on nanomaterials for disease treatment, Adv. Sci. 8 (2021) 2002797, https://doi.org/10.1002/advs.202002797.
[16] S. Wang, C.M. McGuirk, A. d'Aquino, J.A. Mason, C.A. Mirkin, Metal-organic framework nanoparticles, Adv Mater 30 (2018) e1800202, https://doi.org/10.1002/adma.201800202.
[17] D. Wang, D. Jana, Y. Zhao, Metal-organic framework derived nanozymes in biomedicine, Acc. Chem. Res. 53 (2020) 1389–1400, https://doi.org/10.1021/acs.accounts.0c00268.
[18] L. Wang, S. Qiu, X. Li, Y. Zhang, M. Huo, J. Shi, Myocardial-targeting tannic cerium nanocatalyst attenuates ischemia/reperfusion injury, Angew Chem. Int. Ed. Engl. 62 (2023) e202305576, https://doi.org/10.1002/anie.202305576.
[19] Y.G. Kim, Y. Lee, N. Lee, M. Soh, D. Kim, T. Hyeon, Ceria-based therapeutic antioxidants for biomedical applications, Adv Mater 36 (2024) e2210819, https://doi.org/10.1002/adma.202210819.
[20] M.A. Saifi, S. Seal, C. Godugu, Nanoceria, the versatile nanoparticles: promising biomedical applications, J Control Release 338 (2021) 164–189, https://doi.org/10.1016/j.jconrel.2021.08.033.
[21] D. Ni, H. Wei, W. Chen, Q. Bao, Z.T. Rosenkrans, T.E. Barnhart, C.A. Ferreira, Y. Wang, H. Yao, T. Sun, D. Jiang, S. Li, T. Cao, Z. Liu, J.W. Engle, P. Hu, X. Lan, W. Cai, Ceria nanoparticles meet hepatic ischemia-reperfusion injury: the perfect imperfection, Adv Mater 31 (2019) e1902956, https://doi.org/10.1002/adma.201902956.
[22] L. Zhou, S. Tang, F. Li, Y. Wu, S. Li, L. Cui, J. Luo, L. Yang, Z. Ren, J. Zhang, D. Zhou, J. Jiang, X. Yang, X. Zhou, Y. Wu, Ceria nanoparticles prophylactic used for renal ischemia-reperfusion injury treatment by attenuating oxidative stress and inflammatory response, Biomaterials 287 (2022) 121686, https://doi.org/10.1016/j.biomaterials.2022.121686.
[23] A. Khurana, P. Anchi, P. Allawadhi, V. Kumar, N. Sayed, G. Packirisamy, C. Godugu, Superoxide dismutase mimetic nanoceria restrains cerulein induced acute pancreatitis, Nanomedicine (Lond). 14 (2019) 1805–1825, https://doi.org/10.2217/nnm-2018-0318.
[24] A. Khurana, M.A. Saifi, C. Godugu, Nanoceria ameliorates fibrosis, inflammation, and cellular stress in experimental chronic pancreatitis, ACS Biomater. Sci. Eng. 9 (2023) 1030–1042, https://doi.org/10.1021/acsbiomaterials.2c00933.
[25] S. Liang, X.L. Wu, J. Xiong, X. Yuan, S.L. Liu, M.H. Zong, W.Y. Lou, Multivalent Ce-MOFs as biomimetic laccase nanozyme for environmental remediation, Chem Eng J 450 (2022), https://doi.org/10.1016/j.cej.2022.138220.
[26] M. Lammert, C. Glissmann, H. Reinsch, N. Stock, Synthesis and characterization of new Ce(IV)-MOFs exhibiting various framework topologies, Cryst. Growth Des. 17 (2017) 1125–1131, https://doi.org/10.1021/acs.cgd.6b01512.
[27] G.Y. Liou, H. Döppler, U.B. Braun, R. Panayiotou, M. Scotti Buzhardt, D.C. Radisky, H.C. Crawford, A.P. Fields, N.R. Murray, Q.J. Wang, M. Leitges, P. Storz, Protein kinase D1 drives pancreatic acinar cell reprogramming and progression to intraepithelial neoplasia, Nat. Commun. 6 (2015) 6200, https://doi.org/10.1038/ncomms7200.

[28] G.Y. Liou, H. Doppler, B. Necela, B. Edenfield, L. Zhang, D.W. Dawson, P. Storz, Mutant KRAS-induced expression of ICAM-1 in pancreatic acinar cells causes attraction of macrophages to expedite the formation of precancerous lesions, Cancer Discov. 5 (2015) 52–63, https://doi.org/10.1158/2159-8290.CD-14-0474.
[29] J. Shan, L. Du, X. Wang, S. Zhang, Y. Li, S. Xue, Q. Tang, P. Liu, Ultrasound trigger Ce-based MOF nanoenzyme for efficient thrombolytic therapy, Adv. Sci. 11 (2024) e2304441, https://doi.org/10.1002/advs.202304441.
[30] Z.X. Chen, Z. Li, N.N. Tang, Y.D. Huang, S.H. Li, W.J. Xu, Q. Wang, X. Chen, N. Zhao, Z.H. Zeng, Y.C. Xiao, X.Y. Chen, J.W. Li, X.T. Zhou, G.S. Li, M. Yang, J. H. Huang, Engineering ultra-small cerium-based metal-organic frameworks nanozymes for efficient antioxidative treatment of dry eye disease, Adv. Funct. Mater. 34 (2024), https://doi.org/10.1002/adfm.202307569.
[31] W. Liang, H. Xu, F. Carraro, N.K. Maddigan, Q. Li, S.G. Bell, D.M. Huang, A. Tarzia, M.B. Solomon, H. Amenitsch, L. Vaccari, C.J. Sumby, P. Falcaro, C.J. Doonan, Enhanced activity of enzymes encapsulated in hydrophilic metal-organic frameworks, J. Am. Chem. Soc. 141 (2019) 2348–2355, https://doi.org/10.1021/jacs.8b10302.
[32] G.S. Shadel, T.L. Horvath, Mitochondrial ROS signaling in organismal homeostasis, Cell 163 (2015) 560–569, https://doi.org/10.1016/j.cell.2015.10.001.
[33] M. Gutierrez-Aguilar, C.P. Baines, Structural mechanisms of cyclophilin D-dependent control of the mitochondrial permeability transition pore, Biochim. Biophys. Acta 1850 (2015) 2041–2047, https://doi.org/10.1016/j.bbagen.2014.11.009.
[34] A. Dikalova, D. Fehrenbach, V. Mayorov, A. Panov, M. Ao, L. Lantier, V. Amarnath, M.G. Lopez, F.T.t. Billings, M.N. Sack, S. Dikalov, Mitochondrial CypD acetylation promotes endothelial dysfunction and hypertension, Circ. Res. 134 (2024) 1451–1464, https://doi.org/10.1161/CIRCRESAHA.123.323596.
[35] Z. Ma, W. Xie, T. Luo, Z. Hu, J. Hua, J. Zhou, T. Yang, W. Wang, Z. Song, X. Yu, J. Xu, S. Shi, Exosomes from TNF-alpha preconditioned human umbilical cord mesenchymal stromal cells inhibit the autophagy of acinar cells of severe acute pancreatitis via shuttling bioactive metabolites, Cell. Mol. Life Sci. 80 (2023) 257, https://doi.org/10.1007/s00018-023-04861-1.
[36] W. Xie, T. Luo, Z. Ma, S. Xue, X. Jia, T. Yang, Z. Song, Tumor necrosis factor alpha preconditioned umbilical cord mesenchymal stem cell-derived extracellular vesicles enhance the inhibition of necroptosis of acinar cells in severe acute pancreatitis, Tissue Eng. 29 (2023) 607–619, https://doi.org/10.1089/ten.TEA.2023.0139.
[37] P. Sulkshane, J. Ram, A. Thakur, N. Reis, O. Kleifeld, M.H. Glickman, Ubiquitination and receptor-mediated mitophagy converge to eliminate oxidation-damaged mitochondria during hypoxia, Redox Biol. 45 (2021) 102047, https://doi.org/10.1016/j.redox.2021.102047.
[38] Z. Ma, J. Zhou, T. Yang, W. Xie, G. Song, Z. Song, J. Chen, Mesenchymal stromal cell therapy for pancreatitis: progress and challenges, Med. Res. Rev. 41 (2021) 2474–2488, https://doi.org/10.1002/med.21801.
[39] G. Song, J. Zhou, R. Song, D. Liu, W. Yu, W. Xie, Z. Ma, J. Gong, H. Meng, T. Yang, Z. Song, Long noncoding RNA H19 regulates the therapeutic efficacy of mesenchymal stem cells in rats with severe acute pancreatitis by sponging miR-138-5p and miR-141-3p, Stem Cell Res. Ther. 11 (2020) 420, https://doi.org/10.1186/s13287-020-01940-z.
[40] V.K. Singh, D. Yadav, P.K. Garg, Diagnosis and management of chronic pancreatitis: a review, JAMA 322 (2019) 2422–2434, https://doi.org/10.1001/jama.2019.19411.
[41] E. Toth, J. Maleth, N. Zavogyan, J. Fanczal, A. Grassalkovich, R. Erdos, P. Pallagi, G. Horvath, L. Tretter, E.R. Balint, Z. Rakonczay Jr., V. Venglovecz, P. Hegyi, Novel mitochondrial transition pore inhibitor N-methyl-4-isoleucine cyclosporin is a new therapeutic option in acute pancreatitis, J Physiol. 597 (2019) 5879–5898, https://doi.org/10.1113/JP278517.
[42] T. Liu, B. Xiao, F. Xiang, J. Tan, Z. Chen, X. Zhang, C. Wu, Z. Mao, G. Luo, X. Chen, J. Deng, Ultrasmall copper-based nanoparticles for reactive oxygen species scavenging and alleviation of inflammation related diseases, Nat. Commun. 11 (2020) 2788, https://doi.org/10.1038/s41467-020-16544-7.
[43] X. Li, Y. Liu, X. Qi, S. Xiao, Z. Xu, Z. Yuan, Q. Liu, H. Li, S. Ma, T. Liu, Y. Huang, X. Zhang, X. Zhang, Z. Mao, G. Luo, J. Deng, Sensitive activatable nanoprobes for real-time ratiometric magnetic resonance imaging of reactive oxygen species and ameliorating inflammation in vivo, Adv Mater 34 (2022) e2109004, https://doi.org/10.1002/adma.202109004.
[44] J. Yang, B. Ren, X. Yin, L. Xiang, Y. Hua, X. Huang, H. Wang, Z. Mao, W. Chen, J. Deng, Expanded ROS generation and hypoxia reversal: excipient-free self-assembled nanotheranostics for enhanced cancer photodynamic immunotherapy, Adv Mater 36 (2024) e2402720, https://doi.org/10.1002/adma.202402720.
[45] X. Jiang, J. Wei, X. Ding, K. Zheng, T. Zhou, J. Shi, H. Lai, S. Qian, X. Zhang, From ROS scavenging to boosted osseointegration: cerium-containing mesoporous bioactive glass nanoparticles functionalized implants in diabetes, J Nanobiotechnology 22 (2024) 639, https://doi.org/10.1186/s12951-024-02865-y.
[46] Y. Peng, J. Hong, D. Raftery, Q. Xia, D. Du, Metabolomic-based clinical studies and murine models for acute pancreatitis disease: a review, Biochim. Biophys. Acta, Mol. Basis Dis. 1867 (2021) 166123, https://doi.org/10.1016/j.bbadis.2021.166123.
[47] C.H. Kubisch, M.D. Sans, T. Arumugam, S.A. Ernst, J.A. Williams, C.D. Logsdon, Early activation of endoplasmic reticulum stress is associated with arginine-induced acute pancreatitis, Am. J. Physiol. Gastrointest. Liver Physiol. 291 (2006) G238–G245, https://doi.org/10.1152/ajpgi.00471.2005.